



AMERICAN METEOROLOGICAL SOCIETY

Journal of Climate

EARLY ONLINE RELEASE

This is a preliminary PDF of the author-produced manuscript that has been peer-reviewed and accepted for publication. Since it is being posted so soon after acceptance, it has not yet been copyedited, formatted, or processed by AMS Publications. This preliminary version of the manuscript may be downloaded, distributed, and cited, but please be aware that there will be visual differences and possibly some content differences between this version and the final published version.

The DOI for this manuscript is doi: 10.1175/JCLI-D-18-0151.1

The final published version of this manuscript will replace the preliminary version at the above DOI once it is available.

If you would like to cite this EOR in a separate work, please use the following full citation:

Lintner, B., and W. Boos, 2019: Using atmospheric energy transport to quantitatively constrain South Pacific Convergence Zone shifts during ENSO. *J. Climate*. doi:10.1175/JCLI-D-18-0151.1, in press.



**Using atmospheric energy transport to quantitatively constrain South Pacific Convergence
Zone shifts during ENSO**

Benjamin R. Lintner^{1,2}, and William R. Boos^{3,4}

Revised for *Journal of Climate*

14 January 2019

¹*Rutgers, The State University of New Jersey, New Brunswick, NJ, USA*

²*Rutgers Institute of Earth, Ocean, and Atmospheric Sciences, New Brunswick, NJ, USA*

³*University of California, Berkeley, CA, USA*

⁴*Lawrence Berkeley National Laboratory, Berkeley, CA, USA*

*Corresponding author: Benjamin R. Lintner, Rutgers, The State University of New Jersey,
Department of Environmental Sciences, 14 College Farm Road, New Brunswick, NJ 08901-
8551, USA

Email: lintner@envsci.rutgers.edu

Abstract. The South Pacific Convergence Zone (SPCZ) exhibits well-known spatial displacements in response to anomalous sea surface temperatures (SSTs) associated with the El Niño/Southern Oscillation (ENSO). Although dynamic and thermodynamic changes during ENSO events are consistent with observed SPCZ shifts, explanations for these displacements have been largely qualitative. This study applies a theoretical framework based on generalizing arguments about the relationship between the zonal-mean Intertropical Convergence Zone (ITCZ) and atmospheric energy transport (AET) to 2D, permitting quantification of SPCZ displacements during ENSO. Using either resolved atmospheric energy fluxes or estimates of column-integrated moist energy sources, this framework predicts well the observed SPCZ shifts during ENSO, at least when anomalous ENSO-region SSTs are relatively small. In large-amplitude ENSO events, such as the 1997-1998 El Niño, the framework breaks down because of the large change SPCZ precipitation intensity. The AET framework permits decomposition of the ENSO forcing into various components, e.g., column radiative heating vs. surface turbulent fluxes, and local vs. remote contributions. Column energy source anomalies in the equatorial central and eastern Pacific dominate the SPCZ shift. Furthermore, although the radiative flux anomaly is larger than the surface turbulent flux anomaly in the SPCZ region, the radiative flux anomaly, which can be viewed as a feedback on the ENSO forcing, accounts for slightly less than half of SPCZ precipitation anomalies during ENSO. This study also introduces an idealized analytical model used to illustrate AET anomalies during ENSO and to obtain a scaling for the SPCZ response to an anomalous equatorial energy source.

1. Introduction

The South Pacific Convergence Zone (SPCZ) is a diagonally-oriented band of precipitating deep convection extending from the equatorial western Pacific to the Southern Hemisphere (SH) midlatitudes of the Central Pacific (see Fig. 1). SPCZ precipitation exhibits significant variability across a range of timescales, with this variability having significant implications locally and remotely. The SPCZ strongly impacts the human and natural systems of many island nations in the South Pacific (Murphy et al. 2014). For example, the poleward edge of the SPCZ represents a location for tropical cyclogenesis, with changes in SPCZ position or intensity modulating tropical cyclone formation, tracks, and intensity (Vincent et al. 2011). Moreover, variability within the SPCZ may induce variability in the mid- and high-latitudes of the Southern Hemisphere via atmospheric teleconnections (Clem and Renwick, 2015).

The El Niño/Southern Oscillation (ENSO) accounts for much of the observed interannual variability of SPCZ rainfall (Trenberth 1976; Folland et al. 2002; Widlansky et al. 2011). Matthews et al. (1996) and Matthews (2012) further demonstrated variability of SPCZ rainfall on intraseasonal timescales related to the occurrence of active phases of the Madden-Julian Oscillation (MJO) in the vicinity of Indonesia, while Niznik et al. (2015) emphasized the role of synoptic-scale interactions with SH midlatitude disturbances. In fact, the variability of SPCZ convection often reflects interactions across multiple timescales, e.g., the phase of ENSO or the MJO may modify the behavior of synoptic scale interactions with SPCZ convection (Matthews 2012). Kidwell et al. (2016) examined various metrics for characterizing SPCZ variability (e.g., intensity, areal extent, centroid latitude) and found that these metrics behave differently depending on the timescale of the variability.

SPCZ variability in response to ENSO, the primary focus of this study, has been typically interpreted in terms of spatial displacements of the entire SPCZ rain band or its axis of maximum precipitation. However, studies have drawn somewhat different conclusions about the nature of these SPCZ displacements. For example, Salinger et al. (2014) identify eastward displacements of the SPCZ from sea level pressure data on the order of 1-3° during El Niño and westward displacements of similar magnitude during La Niña. On the other hand, Haffke and Magnusdottir (2013) suggest that, while the SPCZ shifts primarily northward during El Niño events, it also frequently assumes a more zonal orientation. During some El Niño events, the SPCZ and eastern Pacific Intertropical Convergence Zone (ITCZ) effectively merge near the equator, leading to so-called zonal SPCZs, while in others the SPCZ and ITCZ remain distinct (Vincent et al. 2011; Borlace et al. 2014). Choi et al. (2015) applied an iterative procedure to decompose tropical Pacific precipitation anomalies during ENSO into meridional and zonal shifts and concluded from this that more than 90% of the anomalous precipitation signature during ENSO can be attributed to such displacements, as opposed to changes in precipitation intensity or amplitude. Analyzing a multidecadal record of 20th century SPCZ displacements recorded in sea surface salinity, Juillet-Leclerc et al. (2006) show that prior to 1970, the SPCZ experienced relatively few ENSO-related spatial displacements, but since that time, such displacements have become more commonplace.

Forcing of SPCZ precipitation by ENSO has been attributed to both anomalous sea surface temperatures (SSTs) and associated atmospheric processes (Lorrey et al. 2012). One way of understanding the SST impact is through regulation of low-level moist static energy (MSE). In particular, during El Niño events, when SSTs are anomalously warm throughout the eastern and central equatorial Pacific, low-level MSE increases, through the effect of increases in both

temperature and moisture in the boundary layer (Neelin and Held, 1987). Enhanced low-level MSE during El Niño may be expected to support precipitating deep convection in the otherwise climatologically unfavorable region for deep convection (in a thermodynamic sense) located to the northeast of the SPCZ. Takahashi and Battisti (2007) and Lintner and Neelin (2008) also highlight the potential role of southeasterly trade wind variability, particularly in determining the position of the eastern margin of the SPCZ: with the slackened trades during El Niño, horizontal advection of relatively low MSE (cool and dry) air into the SPCZ from the southeastern tropical Pacific is suppressed, which supports convection occurring to the east of its mean position. Other studies, particularly at high frequencies, have emphasized upper-level forcing associated with extratropical-tropical interactions, Rossby wave dynamics, and equatorial waves (Matthews et al. 1996; Widlansky 2011; Matthews 2012)

While past work has no doubt provided much insight into potential physical mechanisms underlying the SPCZ spatial displacements, many of the studies have been largely qualitative. What we seek is a more quantitatively-oriented framework, to address how much the SPCZ shifts in response to ENSO forcing. Furthermore, we aim eventually to develop a theory that predicts these shifts given the ENSO-related changes in SST, rather than merely diagnosing them from variables such as MSE that already include the atmospheric response. To that end, in this study, we diagnose SPCZ displacements associated with ENSO in the context of divergent atmospheric energy transport (AET), following an approach developed by Boos and Korty (2016), hereafter BK2016. As we discuss further in Section 4, the BK2016 framework generalizes to two dimensions (latitude and longitude) prior vertically integrated energy budget theories for the latitude of the zonal-mean ITCZ position (e.g., Broccoli et al. 2006; Kang et al.

2008; Donohoe et al. 2013; Bischoff and Schneider 2014). A related energy-budget perspective on zonally-varying meridional shifts in the ITCZ was presented by Adam et al. (2016).

To be clear, theory relating precipitation changes to column energy sources via the vertically integrated atmospheric energy budget dates back to Neelin and Held (1987), who used that framework to understand aspects of the atmospheric changes occurring during ENSO; the Neelin-Held framework, however, emphasized the control of precipitation by local changes in both column energy sources and a moist stability (the “gross moist stability”). More recent energy budget frameworks, including BK2016, quantify rainfall spatial displacements in response to remote changes in column energy sources and do not require specification of a gross moist stability; these frameworks are, however, more limited in that they quantify only precipitation shifts and not changes in precipitation amplitude.

Despite such limitations, we choose to apply an energetics framework here because it goes beyond the more qualitative notion of the SPCZ rainfall shifting in response to, e.g., upstream MSE or trade wind perturbations, as in previous studies. Under this framework, it is possible to diagnose ENSO-related SPCZ displacements in terms of contributions from component processes or mechanisms, such as surface turbulent fluxes vs. column radiative fluxes, as we show further below. Note that our emphasis on AET does not exclude the potentially important contribution of ocean dynamics in generating the distribution of tropical rainfall, as suggested by studies using coupled ocean-atmosphere models (Kang et al. 2018). However, our work contrasts with previous studies that quantified ocean feedbacks on the atmospheric response to an exogenous forcings (e.g. Green and Marshall 2017, Schneider 2017) in that we essentially use the atmospheric energy budget to obtain the tropical rainfall response caused by the ocean dynamical changes occurring in ENSO. In other words, we seek the direct atmospheric response

to a given change in ocean surface evaporation, as well as the indirect atmospheric response resulting from radiative feedbacks on that ocean forcing. More generally, our approach provides an example of how energetic constraints can be useful in elucidating and interpreting regional climate variability, which echoes the recommendation of a recent review by Biasutti et al. (2018) for continuing applications of such constraints to diagnose the behavior of monsoon systems and regional rainbands in the tropics.

2. Data

We analyze observed monthly-mean precipitation data from the Climate Prediction Center (CPC) Merged Analysis of Precipitation (CMAP; Xie and Arkin 1997), provided by NOAA/OAR/ESRL PSD, Boulder, Colorado, USA, from their web site at <http://www.esrl.noaa.gov/psd> for austral summer (December-January-February, or DJF) 1979-2016. Austral summer is the season during which SPCZ convection is most intense and its areal extent is maximized (Vincent 1994). Austral summer also corresponds to the season when ENSO events typically reach maturity. We distinguish DJFs based on ENSO phases defined according to the Oceanic Nino Index (ONI), and following the CPC phase categorizations for three month intervals, summarized in Table 1. DJFs are designated by the year of January, e.g., 1980 refers to December 1979-February 1980. Apart from spanning a range of ONI values, the ENSO events analyzed here encompass different flavors of ENSO, e.g., so-called Eastern Pacific (EP) and Central Pacific (CP) types (Kao and Yu, 2009). The richness of ENSO diversity should be kept in mind when interpreting the SPCZ or other regional responses, as details such as the spatial distribution of SST anomalies during ENSO events may exert a strong impact on the regional manifestation of ENSO-related variability (Capotondi et al. 2015; Yeh et al. 2018).

We obtain atmospheric energy fluxes from ERA-Interim (Dee et al. 2011), the most recent reanalysis of the European Centre for Medium-Range Weather Forecasts (ECMWF). Specifically, we use monthly mean atmospheric moist energy fluxes, vertically integrated over the full depth of the atmosphere, for 1979-2016, as provided by the National Center for Atmospheric Research (<http://climatedataguide.ucar.edu/climate-data/era-interim-derived-components>). These fluxes are derived from 6-hourly estimates of the atmospheric state after eliminating the residual from the vertically integrated, time-dependent mass budget for each 6-hourly state estimate by subtracting a barotropic wind from the horizontal wind at each level (Trenberth 1997; Trenberth et al. 2001). Doing so eliminates any column-integrated mass budget residual caused by analysis tendencies, sampling, or numerics via a barotropic correction; the corrected winds are then used to calculate vertically integrated, monthly mean atmospheric energy fluxes. For reference, we note that previous studies have documented the magnitude of the column-integrated energy budget residuals in ERA-Interim. In the global mean, the mass-adjusted energy budget residual in the ERA-Interim reanalysis itself is 8 Wm^{-2} (Berrisford et al. 2011); Trenberth et al. (2001) found that the native model-level column-integrated energy flux divergence could be replicated to within about 2 Wm^{-2} over ocean. We use vertically integrated energy fluxes computed via the Trenberth et al. methodology, and so expect a similar level (i.e. order 10 Wm^{-2}) of error. Residuals of this size are modest compared to the order 50 Wm^{-2} anomalies in surface and radiative fluxes that occur during ENSO (see Fig 10).

Here we consider averages of monthly mean fluxes of total energy (including latent heat and kinetic energy) over DJF of El Niño and La Niña years to obtain the respective composites. The same procedure is used to obtain the vertically integrated fluxes of dry static energy and of moisture. We also use estimates of the source of moist energy to each atmospheric column, as

given in ERA-Interim. As described in the next section, this source comprises the sum of surface sensible heat flux, surface latent heat flux, and net radiative flux convergence integrated over the depth of the atmosphere. Unlike the energy fluxes described in the previous paragraph, which are obtained from analyzed winds, temperature, humidity, and pressure, this column energy source is less directly constrained by observations.

In several of our analyses presented below, we assess statistical significance through an iterative bootstrapping procedure. In each iteration, we perform the selected analysis using a random sampling of four El Niño events and four La Niña events; 2000 iterations are obtained and the result of an analysis at a particular horizontal point is deemed statistically significant when the 2.5th and 97.5th percentiles of the sampling distribution have the same sign. Note that because of the small number of ENSO events involved, this procedure may overestimate significance, but the conclusions of our analysis are unlikely to be impacted by this.

3. Overview of the SPCZ response to ENSO

Fig. 1 illustrates the austral summer composite difference of CMAP precipitation for El Niño minus La Niña phase conditions (shading); for reference, the DJF climatology over all years is also depicted (line contours). The composite difference exhibits the well-known spatial pattern of ENSO in the Pacific region, with anomalously high precipitation close to the equator over the Central and Eastern Pacific and anomalously low precipitation in the surrounding “horseshoe” over the Western Pacific. The leading mode of an empirical orthogonal function analysis over this region yields a spatial pattern very similar to Fig. 1 (not shown). Within the SPCZ specifically, positive and negative anomalies occur, respectively, to the northeast and southwest of the axis of highest climatological DJF rainfall.

To further quantify and interpret the SPCZ response to ENSO, we analyze the behavior of the precipitation sampled along the cross-SPCZ transect highlighted in Fig. 1. The behavior described below is relatively insensitive to the precise orientation or location of this transect, as long as it crosses the core of the SPCZ equatorward of 15°S . Poleward of this latitude, the slope of the SPCZ, i.e., the change in the rain band's latitude with longitude, is steeper and the maximum rainfall is reduced, as seen by the more north-south orientation of the climatological isohyets. This portion of the SPCZ is subject to stronger influences from transient midlatitude disturbances than is the more tropical portion (Niznik and Lintner 2013; van der Wiel et al. 2015; Niznik et al. 2015).

Fig. 2a illustrates the interannual timeseries of standardized DJF ONI (black), maximum precipitation rates along the cross-SPCZ transect (MAX; green) and locations of the maximum precipitation along the transect (LOC; orange). Each timeseries is standardized by normalizing by its interannual standard deviation and is thus dimensionless. Both MAX and LOC covary with ONI ($r = 0.62$ and $r = 0.77$, respectively, $p < 0.01$): for a +1K anomaly in ONI, MAX increases by 1.3 mm/day, while LOC moves 1.5° to the east/ 1.1° to the north along the transect. MAX and LOC are, of course, mutually significantly correlated ($r = 0.58$, $p < 0.01$). However, the quantitative sensitivities of the responses of SPCZ intensity and location to ENSO vary with the amplitude of ONI anomalies. In particular, excluding from the regression the three largest El Niño events over the period analyzed, i.e., 1983, 1998, and 2016, decreases the correlation between MAX and ONI ($r = 0.46$, $p < 0.01$) and reduces the regression slope (1.0 mm/day/K), while the correlation of LOC and ONI remains approximately the same, with a slight increase in the regression slope (1.6° lon/K). It is worth noting the rather large negative excursion of LOC in 2000, which occurred under La Niña conditions. During this particular DJF, the rainfall over

the SPCZ region was anomalously low, and the precipitation along the transect exhibited two maxima. Because the more westward (poleward) maximum exceeded the more eastward (equatorward) maximum, LOC in 2000 is determined by the westward maximum, although the eastward maximum is closer to the location of peak rainfall during other La Niña events. Defining a weighted location would reduce the prominence of this particular anomaly.

Composites of the cross-SPCZ transect rainfall profiles for neutral, El Niño, and La Niña years are depicted in Fig 2b. For comparison, we have also shifted the neutral year profile along the transect by an amount that minimizes the root mean square difference with respect to either the El Niño or La Niña composite profiles (dashed lines). Overall, shifting the neutral phase profiles agrees well with the profiles occurring during El Niño or La Niña conditions, although the shifted profile underestimates the amplitude during El Niño and overestimates it during La Niña. For the precipitation along the transect corresponding to the three strongest El Niño events (squares), shifting of the neutral phase profile much less adequately captures the observed behavior, as the amplitude of the strong El Niño profile exceeds the neutral phase profile by ~35%. These results illustrate the extent to which the SPCZ changes during ENSO forcing may be viewed as a spatial displacement of precipitation rather than a change in precipitation intensity: although ENSO affects both the position of maximum SPCZ rainfall and its intensity, the former is more strongly affected, especially when the strongest El Niño events are excluded. Qualitatively, this simple demonstration agrees with the more general analysis of the decomposition of tropical Pacific precipitation anomalies into zonal and meridional shifts of Choi et al. (2015).

Having quantified the observed SPCZ shifts for ENSO events, we now turn to application of the quantitative theory of SPCZ displacements based on constraints imposed by AET applied in 2D, following BK2016. In the next section, we review the principal features of this framework.

4. Review of 2D energy budget constraints

The notion of connecting the position of regions of tropical rainfall to remote energy sources may be traced to studies linking meridional shifts in the zonal-mean Intertropical Convergence Zone (ITCZ) to interhemispheric imbalances in atmospheric energy sources, which were developed largely in the context of paleoclimate (e.g. Chiang and Bitz 2005; Broccoli et al. 2006). According to this paradigm, the presence of a positive anomalous energy source in one hemisphere leads to the development of an anomalous cross-equatorial Hadley circulation, which acts to reduce interhemispheric thermal imbalance through net export of energy from the warmer to cooler hemisphere. With anomalous displacement of the rising branch of the Hadley circulation toward the positive anomalous energy source, the net flux of dry static energy from the warmer to cooler hemisphere is enhanced. Since the zonal-mean ITCZ lies in the rising branch of the Hadley circulation, it too migrates toward the heating anomaly. Current-day observations and paleoclimate model simulations indicate northward displacement of the zonal-mean ITCZ of $\sim 3^\circ$ latitude for every 10^{15} W (1 petawatt or PW) of anomalous net southward energy transport across the equator (Donohoe et al. 2013; Bischoff and Schneider 2014).

Recent efforts, including BK2016 and Adam et al. (2016), have sought to extend application of the zonal-mean ITCZ-AET framework to 2-dimensions, in latitude and longitude, in order to interpret shifts in regional rainfall features. The motivation for doing so is that the zonal-mean ITCZ is itself an average over distinct regional ITCZs and monsoonal/continental precipitation

maxima. Such regional-scale precipitation maxima may exhibit greater sensitivity to climate forcing than the zonal-mean ITCZ, e.g., estimates of regional shifts derived from paleoproxies for both the mid-Holocene and Last Glacial Maximum indicate anomalous meridional excursions of 5° or more, while for the same periods, the zonal-mean ITCZ is estimated to have shifted by less than 1° latitude (McGee et al. 2014). Moreover, zonal shifts in precipitation may be as large as or even exceed meridional shifts, which may greatly affect the interpretation of localized variations in hydroclimate.

Generalizations of these ideas to two dimensions (Adam et al. 2016; BK2016) proceed by introducing an MSE flux potential, χ , which is related to the (horizontal) divergence of column-integrated MSE transport via Poisson's equation:

$$\nabla^2 \chi = \nabla \cdot \langle h \mathbf{u} \rangle \quad (1)$$

where \mathbf{u} is the horizontal wind, $h = c_p T + L_v q + \Phi$ is the MSE, $\Phi = gz$ is the geopotential, g is gravitational acceleration, and $\langle \dots \rangle$ indicates mass-weighted vertical integration over the atmosphere from surface pressure p_s to the top-of-the-atmosphere (at $p = 0$), i.e., $\langle \dots \rangle = \int_0^{p_s} \dots \frac{dp}{g}$. We denote the horizontal divergent component of the column-integrated MSE transport as $(\partial_x \chi, \partial_y \chi) = (u_h, v_h)$, with all derivatives evaluated in spherical coordinates but written here in Cartesian coordinates for simplicity.

For a meridional overturning circulation, the ascending branch of the circulation occurs along an energy flux equator (EFE), i.e., a latitude for which $v_h = 0$ and $\partial_y v_h > 0$. Similarly, for a zonal overturning circulation, the ascending branch occurs along an energy flux prime meridian (EFPM), a longitude for which $u_h = 0$ and $\partial_x u_h > 0$. The essential assumption of the BK2016 framework is that spatial displacements in the tropical precipitation field follow spatial displacements of the EFE or EFPM, that is, it is a 2D analogue to the zonal-mean EFE. Thus, for

two climate states differing in terms of the spatial positions of their EFEs and/or EFPMs, a simple remapping relates the precipitation fields of the two states, i.e.,

$$P_2(\phi - \phi', \lambda - \lambda') = P_1(\phi, \lambda) \quad (2)$$

Here, the latitude and longitude shifts, ϕ' and λ' , are given by:

$$\phi' = (\phi_{0,2} - \phi_{0,1})\Theta(\Delta\phi - |\phi - \phi_{0,1}|) \quad (3)$$

$$\lambda' = (\lambda_{0,2} - \lambda_{0,1})\Theta(\Delta\lambda - |\lambda - \lambda_{0,1}|)$$

where $\phi_{0,i}$ and $\lambda_{0,i}$ denote, respectively, the latitude of the EFE and the longitude of the EFPM in climate state i , Θ is the Heaviside function, and $\Delta\phi$ and $\Delta\lambda$ are zonal and meridional intervals over which shifts are computed (i.e., $\Delta\phi = 20^\circ$ latitude and $\Delta\lambda = 80^\circ$ longitude specify the range of influence of the EFE or EFPM shifts). Note that $\phi_{0,i}$ and $\lambda_{0,i}$ are functions of longitude and latitude, respectively. Under conditions for which multiple EFEs exist at a given longitude, a mean ϕ' is computed; multiple EFPMs at a given latitude are treated analogously.

While equation (1) provides a direct approach for computing χ , and hence the divergent AET, from winds and MSE, it is further possible to compute χ using sources (and sinks) of MSE, or the energy fluxes into (and out of) the column. To see this, consider the vertically-integrated MSE equation, which can be obtained by combining the vertically-integrated atmospheric thermodynamic and moisture conservation equations (see Neelin 2007):

$$\partial_t \langle c_p T + L_v q \rangle + \langle \mathbf{u} \cdot \nabla (c_p T + L_v q) \rangle + \langle \omega \partial_p h \rangle = E + H + R \quad (4)$$

where the terms on the right-hand side are (surface) latent heat flux E , sensible heat flux H , and column radiative heating R , the latter comprising both shortwave and longwave contributions at both the top-of-the-atmosphere and surface. Assuming steady-state conditions, applying continuity $\nabla \cdot \mathbf{u} + \partial_p \omega = 0$, and integrating the vertical advection term by parts, equation (4) becomes:

$$\langle \nabla \cdot (h\mathbf{u}) \rangle - \langle \mathbf{u} \cdot \nabla \phi \rangle = E + H + R \quad (5)$$

The 2nd term on the left-hand side is the vertically-integrated horizontal advection of geopotential. Combining (1) and (5) and neglecting advection of geopotential, which represents a (relatively small) rate of conversion to kinetic energy, we have:

$$\nabla^2 \chi \approx E + H + R \quad (6)$$

The linearity of equation (6) implies that χ can be decomposed into additive contributions of each of the energy source terms on the RHS; we will make use of this property below.

5. SPCZ response to ENSO in the energy budget framework

As a first application of BK2016 to interpret the observed SPCZ response to ENSO, we solve equation (1) using the resolved thermodynamic and wind fields from ERA-Interim to compute the MSE flux. Fig. 3 depicts the DJF climatological χ and (u_h, v_h) , along with the climatological mean DJF rainfall and the locations of the EFE and EFPM. Note that because of the definition of χ in equation (1), the divergent energy flux is directed up the gradient of χ . Similarly, Fig. 4 shows El Niño minus La Niña composite differences of the MSE flux potential, divergent flux, and rainfall, along with the locations of the EFE and EFPM for both El Niño and La Niña phases (red and blue contours, respectively). Note that for El Niño, we have excluded 1983, 1998, and 2016, since these El Niños involve a much larger change in precipitation amplitude, as demonstrated in Fig. 2b. Incidentally, these excluded El Niño events are all of the eastern Pacific type, although as Paek et al. (2017) note, the 2016 event shared some behavior with the central Pacific type. Similar figures are presented in BK2016, although that study shows annual means and does not explicitly estimate precipitation anomalies by application of

equation (2). Here we briefly review some aspects of the energetics relevant to the ENSO-SPCZ connection.

Climatologically, the western Pacific warm pool represents a region of net divergence of column MSE flux, with net export of energy to higher latitudes as well as zonally within the Tropics. In the western Pacific warm pool, intense heating of the troposphere by deep convection tends to dominate over net radiative cooling (L'Ecuyer and Stephens 2007), leading to the energy export implied by column MSE flux. A secondary minimum in χ , and thus a region of net MSE flux divergence, occurs over tropical South America. In terms of the large-scale circulation, the rising branches of both the large-scale meridional (Hadley) and zonal (Walker) overturning circulations are additive in the western Pacific warm pool region. For El Niño minus La Niña, χ is reduced over the Central and Eastern Pacific and increased over the Western Pacific, in concert with El Niño phase warming of SSTs to the east that ultimately increase the input of energy to the atmospheric column there. The El Niño minus La Niña phase divergent energy flux has a zonal component directed from the eastern to western Pacific.

The climatological EFE for DJF tends to occur in low latitudes of the SH, consistent with the rising branch of the Hadley circulation occurring there in austral summer. The EFE more closely follows the SPCZ over the central Pacific compared to the ITCZ. This correspondence between the EFE and SPCZ rather than the ITCZ may be understood in terms of the differences in character of deep convection in the SPCZ and ITCZ: while low-level convergence is stronger in the ITCZ, SPCZ convection tends to be deeper (Wang and Li 1993) and to produce a larger net column-integrated export of energy (Back and Bretherton 2006; Peters et al. 2008). Two EFPMs are observed, given the occurrence of two tropical maxima in χ .

Applying equation (2) to estimate the precipitation field for El Niño conditions, relative to observed La Niña conditions as a baseline, and subtracting the La Niña composite rainfall yields the difference map depicted in Fig. 5a. Here, significance (as indicated by the stippling) is assessed through a bootstrapping with replacement sampling as discussed in Section 2. Comparing these precipitation anomalies to those depicted in Fig. 4 reveals some common regional features, not only over the SPCZ region but also over the Maritime Continent and northern Indian Ocean and along the Atlantic ITCZ. Fig. 5b highlights the precipitation profiles along the cross-SPCZ transect. The theoretical estimate for El Niño (dashed red line) reasonably matches the observed El Niño profile (solid red line) reasonably, although it slightly underestimates the anomalous precipitation maximum to the northeast and slightly overestimates the minimum to the southwest. In Section 7, we will further deconstruct the SPCZ shift by considering contributions from different processes related to, or different aspects of, the ENSO forcing.

Of course, the theoretical prediction also fails to capture some of the features of the observed precipitation differences between El Niño and La Niña. Most prominently, the theory predicts negative near-equatorial El Niño phase precipitation anomalies along the ITCZ in the northeast tropical Pacific, with positive anomalies just to the north, in stark contrast to the observations, which exhibit anomalies of the opposite sign here. This disagreement occurs because the theory only considers shifts in the zero lines of the divergent energy flux, and the divergent energy flux is nonzero and northward across the East Pacific ITCZ in the basic state (see vectors in Fig. 3). When the MSE source increases in the equatorial East Pacific during El Niño, the northward energy flux across the East Pacific ITCZ increases, corresponding to an equatorward shift in the entire distribution of the meridional energy flux; this shift is in the same direction as the ITCZ

shift (Fig. 6), showing that the theory would be correct if it were based more generally on horizontal shifts in the entire energy flux distribution rather than on the particular shifts of the zero lines of that distribution. In the annual mean, there are two EFEs in the East Pacific during La Niña, one corresponding to the SPCZ and one to the ITCZ, and they both shift toward the equator during El Niño (see Fig. 2d of BK16, and Adam et al. 2016), but in our analyses of the DJF state, there is only one EFE in the southeastern Pacific.¹ Of course, both shifts and changes in amplitude of the full distribution of divergent energy fluxes can be related to circulation changes through the theory introduced by Neelin and Held (1987), but that requires knowledge of the unconstrained gross moist stability. Viewed from a thermodynamic perspective, the equatorward shift of the East Pacific ITCZ during El Niño is consistent with increasing near equatorial low-level MSE. In particular, under La Niña or even neutral conditions, this region is too cool, dry, and stable to support precipitating deep convection. With warming and moistening of the boundary layer there during El Niño, the region becomes thermodynamically favorable in supporting precipitating deep convection.

Another difference between the theoretical prediction and observations involves the predicted regional increase of precipitation along the western coastline of South America and the broad decrease along the eastern coastline. This behavior follows from the El Niño-phase westward displacement of the EFPM crossing South America. Under observed El Niño conditions, above normal rainfall does occur along coasts of Peru and Ecuador, but the anomalies are zonally rather confined. In fact, note that no positive anomalies are evident in this coastal region in Fig. 4

¹ Bischoff and Schneider (2014) discuss a related scenario in which a double ITCZ responds to changes in an equatorial energy source, and use a third-order Taylor expansion to approximate the EFE and ITCZ shifts in terms of changes in the equatorial energy source and equatorial energy flux. However, their treatment still identifies the ITCZ with a zero line of the northward energy flux. Using their third-order expansion would not improve our theory in the East Pacific because we obtain the exact, global distribution of the divergent energy flux anomaly from the anomalous MSE source by inverting the Laplacian.

(which is based on a coarse resolution product). However, it is not unreasonable to expect poor agreement in the west, given the presence of the Andes as a topographical barrier: in fact, the increased western coastal rainfall likely represents a more direct and local thermodynamic response to warming over the eastern Pacific (Bendix and Bendix 2006) that should not be expected to be captured by a theory that only predicts shifts in the rainfall distribution. Moreover, the subtropical southeastern portion of South America typically experiences increased rainfall during El Niño (Carvalho et al. 2004). Over southeastern South America, previous studies have attributed precipitation anomalies during El Niño phase to a forced extratropical Rossby wave train (Carvalho et al. 2004; Grimm and Tedeschi 2009), which is not accounted for by the simple shift framework.

To summarize our findings thus far, although the ENSO shift paradigm based on BK2016 clearly does not account for all regional scale precipitation features, we nonetheless regard the good agreement in the vicinity of the SPCZ as motivating its applicability there. In the next section, we develop a simplified model for the interaction between two linear and uniform MSE sources—one oriented diagonally, corresponding to the SPCZ, and one oriented zonally, corresponding to El Niño conditions—that exhibits shift behavior analogous to what we have seen above.

6. Idealized analytic model for the shift of a linear convection zone in the presence of a linear heating anomaly

We now describe an idealized analytic model that enables further quantitative understanding of the displacement of the SPCZ in the presence of ENSO forcing. Consider a domain in Cartesian coordinates which is infinite in both the zonal (x) and meridional (y) directions, with an equator

435 at $y = 0$ (Fig. 7). We define a mean state comprising an MSE source of strength F_0 applied
 436 over a band of width $2d_l$ oriented an angle α relative to the zonal direction; this mean state
 437 represents the column MSE source associated with the SPCZ. The center of this MSE source
 438 crosses the equator at $x = x_0$ (taken on the left-hand side of the domain in Fig. 7). From Gauss's
 439 Theorem, the mean state divergent MSE flux is given by:

$$440 \quad (u_0, v_0) = F_0 d(x, y) (\sin \alpha, \cos \alpha) \quad (7)$$

441 where

$$442 \quad d(x, y) = \begin{cases} d_l & : y \geq d_l - (x - x_0) \tan \alpha \\ (x - x_0) \sin \alpha + y \cos \alpha & : \text{otherwise} \\ -d_l & : y \leq -d_l - (x - x_0) \tan \alpha \end{cases} \quad (8)$$

443 The MSE flux potential for the mean state is:

$$444 \quad \chi_o = \begin{cases} \frac{1}{2} d^2(x, y) & : |d(x, y)| \leq d_l \\ d_l |d(x, y)| - \frac{1}{2} d_l^2 & : \text{otherwise} \end{cases} \quad (9)$$

445 Note that the center line along the MSE source, where $d(x, y) = 0$, represents both an energy
 446 flux equator (EFE) and an energy flux prime meridian (EFPM) for the mean state (solid gray line
 447 in Fig. 6), since both $\partial_y v_0 > 0$ and $\partial_x u_0 > 0$ in the right half plane bounded by the SPCZ axis.

448 Suppose further that an anomalous MSE source of strength F' is added in a band along the
 449 equator, also of width $2d_l$; this anomalous source is intended to represent MSE forcing
 450 associated with El Niño conditions. Again from Gauss's Theorem, the MSE flux and associated
 451 flux potentials for this MSE source are:

$$452 \quad (u', v') = (0, F') \begin{cases} d_l & : y \geq d_l \\ y & : \text{otherwise} \\ -d_l & : y \leq -d_l \end{cases} \quad (10)$$

$$453 \quad \chi' = \begin{cases} \frac{1}{2} y^2 & : |y| \leq d_l \\ d_l |y| - \frac{1}{2} d_l^2 & : \text{otherwise} \end{cases} \quad (11)$$

The total MSE flux, the sum of (7) and (10), defines the locations of any EFE or EFPMs for the El Niño state; the total MSE flux, along with contours of the total MSE flux potential, the sum of (9) and (11), is also depicted in Fig. 7 (purple arrows and contours, respectively). In the El Niño state, the EFPM remains collocated with the mean SPCZ, since $u' = 0$. On the other hand, the EFE (dashed gray curve) shifts in the El Niño state relative to its position in the mean state, toward the equatorial region of anomalous MSE forcing. Note that in the “wedge” between the SPCZ and El Niño MSE sources, the magnitude of the MSE flux is small compared to regions on either side of these sources, owing to the cancellation of MSE fluxes associated with each source within the wedge region. Assuming a mean state MSE source in the SPCZ of order 75 W/m^2 and an El Niño-related heating (a perturbation MSE source) of order 25 W/m^2 (see Fig. 10 below), both of which are applied over bands of width $2d_l$ (corresponding to 10°), and oriented relative to one another at an angle corresponding to the mean SPCZ slope (18° according to Haffke and Magnusdottir 2013), our analytic model predicts a northward shift of the EFE by $\sim 1.8^\circ$ latitude near the midpoint of the SPCZ diagonal ($\sim 160^\circ\text{W}$).

We can also use the idealized model to examine how the SPCZ responds as the strength of the perturbation MSE source in the equatorial ENSO region varies. Fig. 8 depicts the latitude of the EFE at a particular longitude (here 160°W) as a function of F' , assuming $F_0 = 1$, in units of column MSE source (blue symbols). As expected, for a fixed SPCZ source, the latitude of the EFE shifts equatorward with an increase in the strength of the ENSO region perturbation MSE source. From the mean and perturbation meridional MSE fluxes, v_0 and v' , and for conditions under which the EFE remains within d_l of its mean state position, the EFE occurs at a latitude y satisfying:

$$0 = v_0 + v' = F_0(x - x_0) \sin \alpha \cos \alpha + F_0 y \cos^2 \alpha - F' d_l \quad (12)$$

At a given longitude, differentiating (12) allows us to determine how a change in y scales with a change in F' , which upon rearranging, yields:

$$\frac{\delta\phi}{\delta F'/F_0} = \frac{d_l}{a \cos^2 \alpha} \quad (13)$$

where $y = a\phi$, with a denoting the radius of the earth. The scaling in (13) represents nothing more than a local form of the zonal-mean scaling for ITCZ latitude. That is, since the (southward) energy flux from the ENSO source region is $-F'd_l$ and the divergence of the meridional energy flux from the SPCZ is $F_0 \cos^2 \alpha$, the two quantities are analogous to the zonal-mean scaling given by equation (3) of Bischoff and Schneider (2014). Reformulated with units as in the zonal-mean scaling, the SPCZ shifts equatorward by $\sim 1^\circ$ for every 10 W m^{-2} increase in ENSO region MSE.

It is worth noting that the EFE latitude jumps at a value of $F' = 0.94$ for the illustrated angle of the SPCZ diagonal, which reflects the fact that all of the MSE flux associated with F' is directed meridionally, so a smaller value of F' is able to cancel the meridional component of MSE flux associated with F_0 . By symmetry, however, one might expect a jump to occur at $F_0 = F' = 1$. To reconcile this expectation with the EFE/EFPM framework, we consider the more general problem of ridge detection, where ridges comprise curves defined by the local maxima of a function of N variables in at least one of the $N - 1$ dimensions. To isolate ridges in the MSE flux potential, it is necessary to compute the eigenvalues of its Hessian matrix. The criteria for identifying a ridge can be expressed as:

$$\begin{aligned} \partial_x \chi \partial_y \chi (\partial_{xx} - \partial_{yy}) \chi + ((\partial_y \chi)^2 - (\partial_x \chi)^2) \partial_{xy} \chi &= 0 \\ ((\partial_y \chi)^2 - (\partial_x \chi)^2) (\partial_{xx} - \partial_{yy}) \chi - 4 \partial_x \chi \partial_y \chi \partial_{xy} \chi &> 0 \end{aligned} \quad (14)$$

The latitude of the ridge as a function of F' is indicated by the red symbols in Fig. 8. Significantly, the jump in the ridge latitude occurs at $F' = 1$. For $F' < 1$, the ridge latitude is

slightly poleward of the EFE, while for $F' > 1$, the ridge latitude and EFE are coincident. The above results suggest that following ridge lines in the MSE flux potential may provide a better 2D generalization of the zonal mean EFE theory, albeit with added complexity (i.e., use of the Hessian matrix) that may only be necessary for large values of α . Our cursory examination of ridge line behavior in the observations (not shown) indicates that the EFE and ridge lines shift by roughly similar amounts, so we suggest that the shifts obtained from either method are likely not to differ too much.

Our idealized model could be readily altered by imposing a distribution of ENSO region MSE that has a circular instead of a linear geometry, which may be regarded as a better representation of the spatial distribution of MSE sources during some El Niño events. Another possibility is that the idealized distributions of F' in the toy model could be applied to the distribution of the reanalysis climatological mean MSE sources, allowing for numerical computations of the sensitivity of EFE and EFPM positions to idealized equatorial perturbations in a more realistic basic state. For example, in constructing our model, we have neglected the Pacific ITCZ, although the presence of the ITCZ would certainly affect the mean EFE/EFPM positions.

7. Deconstructing the SPCZ energetics response

One of the advantages of the BK2016 framework is that it permits *a posteriori* diagnosis of regional responses, in the SPCZ or elsewhere, to different aspects or components of the ENSO forcing. In this section, we highlight how several of these aspects of the forcing impact the response.

7a. *Dry static energy vs. latent heat contributions*

The resolved vertically-integrated MSE flux is the sum of vertically-integrated fluxes of dry static energy (DSE) and moisture, or latent heat ($L_v q$). Fig. 9 illustrates El Niño minus La Niña phase flux potentials associated with perturbations in the fluxes of either DSE (Fig. 9a) or $L_v q$ (Fig. 9b). To leading order, the spatial pattern of perturbation flux potential associated with DSE resembles that obtained for MSE (Fig. 4), but with DSE flux potential values of larger magnitude: the spatial standard deviation of the DSE flux potential is 75% larger than the MSE flux potential. By contrast, the perturbation flux potential associated with $L_v q$ effectively opposes that of MSE, also with larger amplitude than that of MSE, though smaller than that of DSE. The opposition of DSE and moisture fluxes is, of course, characteristic of many tropical circulations (Neelin and Held 1987). Describing El Niño-related DSE and $L_v q$ divergence anomalies directly, Mayer et al. (2013) attributed the tendency for the former to exhibit larger values to an in-phase relationship between anomalous radiative flux and moisture convergence, a point to which we return in the next subsection.

Closer inspection of the DSE, $L_v q$, and MSE perturbation flux potentials indicates some subtle differences in their spatial distribution. For DSE, the extrema, 0.33 PW and -0.45 PW, occur near the Philippines (125°E, 8°N) and close to the Dateline along the equator (166°W, 1°S), respectively. The extrema for $L_v q$ are approximately coincident with those for DSE (126°E, 8°N and 170°W, 3°S) but with signs reversed (-0.24 PW and 0.30 PW). By contrast, the extrema for MSE, 0.1 PW and -0.19 PW, occur over the Indian Ocean (91°E, 5°S) and Central Pacific (136°W, 0°N). Differences in the horizontal structure of the DSE and $L_v q$ flux potentials indicate the existence of horizontal variations in the gross moist stability, since the latter can be

expressed as the ratio of the Laplacians of the MSE and $L_v q$ flux potentials (e.g. Raymond et al. 2009).

Because of the relatively large amplitudes of the perturbation flux potentials associated with DSE and $L_v q$, the precipitation shifts computed for each of these components are large enough that one may reasonably question the validity of the perturbation approach, and thus we do not show them. However, it should be noted that during El Niño, the change in DSE supports a northeastward shift of the EFE, and SPCZ, while the change in $L_v q$ supports a southwestward shift. The net shift obtained (as in Fig. 5) is northeastward, reflecting the larger amplitude of DSE over $L_v q$. Of course, how much the SPCZ shifts depends on the degree of cancellation between these, which underscores the need for their accurate estimation.

7b. Column radiative vs. surface turbulent fluxes

ENSO exerts substantial influence on the components of the energy, moisture, and MSE budgets not only locally in the equatorial Pacific source region but across the global tropics (Neelin 2007; Mayer et al. 2013). Additionally, a number of studies have used models in which various components of the surface energy, moisture, or atmospheric MSE budgets are prescribed to climatology or otherwise prevented from adjusting to ENSO to demonstrate more explicitly the impact of particular mechanisms on the climate response to ENSO (Su and Neelin 2002; Neelin et al. 2003; Chiang and Lintner 2005). From equation (6), it is possible to quantify contributions to the perturbation MSE flux potential, and hence the precipitation anomalies that is obtained from application of BK2016, from individual MSE sources to the atmospheric column, i.e., radiative, latent, and sensible components. That is, instead of decomposing the MSE flux divergence into components associated with DSE and moisture, as was done in the previous

section, we will now separate it into components associated with different geographic regions and different physical processes.

Fig. 10 depicts the spatial distribution of the El Niño minus La Niña differences for the sum of anomalous MSE sources (Fig. 10a) as well as the contributions from anomalous surface turbulent fluxes (Fig. 10b) and net column radiative heating ($R_s - R_{toa}$) (Fig. 10c). Tropical surface turbulent fluxes are largely dominated by surface latent heat fluxes associated with evaporation, since anomalous sensible heat fluxes are small over tropical oceans (Fairall et al. 1996). The net radiative heating anomalies are almost entirely produced by the anomalous cloud radiative forcing (CRF), which in turn is dominated by the anomalous longwave CRF. Decomposition of the radiative heating anomaly into clear-sky, CRF, longwave, and shortwave components is not shown here, but the structural similarity of the precipitation anomaly (Fig. 4) and the radiative heating anomaly (Fig. 10c) supports the idea that moisture-radiation effects provide a positive feedback on both the eastward shift of West Pacific precipitation maximum and the northeastward shift of the SPCZ.

Spatially, the anomalous MSE sources induce heating over much of the equatorial tropical Pacific. This is the region of maximum anomalous divergent MSE flux evident in Fig. 4. Though we do not illustrate it explicitly here, the anomalous MSE flux potential estimated from application of equation (5) is nearly identical to the calculation based on the directly resolved anomalous MSE fluxes. Elsewhere in the tropics, the anomalous MSE flux forcing corresponds to a net cooling of the atmosphere. The total anomalous MSE source in the eastern Pacific is dominated by anomalous surface turbulent fluxes (Fig. 10b). In this region, warming of SST during El Niño drives higher rates of evaporation through the thermodynamic component of the latent flux, i.e., saturation specific humidity increases with SST, although weakening of the

trades during ENSO warm phases should offset some of this thermodynamic forcing through reduced turbulent exchange. Over the north tropical Atlantic and western North Pacific, reduced evaporation leads to anomalous tropospheric cooling.

In the equatorial Pacific to the west of the Dateline as well as over the SPCZ region, anomalous column radiative forcing dominates (Fig. 10c). Anomalous warming occurs over the equator and the equatorward margin of the SPCZ, while anomalous cooling occurs over the Philippines and along the poleward margin of the SPCZ. Comparing the spatial distributions of anomalous radiative flux forcing and anomalous precipitation (Fig. 4) highlights the correspondence between column warming (cooling) due to surface radiative flux change and anomalously positive (negative) precipitation. It is worth noting that the interplay between surface radiative forcing and precipitation appears to vary geographically (Colasacco-Thumm 2015) and likely depends on differences in cloud properties and vertical structure (Kubar et al. 2007).

Clear agreement is evident between the El Niño minus La Niña phase precipitation differences estimated from analyzed anomalous MSE flux (Fig. 5) and from anomalous MSE sources (Fig. 11a). Both of the component MSE source contributions considered here, column radiative and surface turbulent fluxes, produce spatial patterns of precipitation anomalies resembling the total (Figs. 11b and 11c, respectively), with some differences following from differences in the distributions of anomalous sources. For example, in the central and eastern Pacific, precipitation anomalies associated with the surface turbulent source dominate. Even in the SPCZ region, precipitation anomalies associated with surface turbulent fluxes are larger than those from column radiation, indicating that while the cloud feedbacks may be large there, they contribute slightly less than half of the SPCZ precipitation anomaly.

613
614 *7c. MSE sources inside and outside of the principal ENSO forcing region*

615 Finally, we estimate the precipitation response based on divergent energy flux potentials
616 computed from anomalous MSE sources which we have restricted to either the principal ENSO
617 source region (10°N-10°S, 160°E-85°W; Fig. 12a) or the rest of the domain excluding this region
618 (Fig. 12b). Note that this definition of ENSO source region is broad compared to indices
619 typically used to define ENSO. Perhaps not surprisingly, MSE sources over the region
620 containing the principal ENSO SST anomalies account for much of the predicted precipitation
621 response in the central and eastern Pacific. For the SPCZ, the MSE forcing from the ENSO
622 region also dominates, although MSE sources over the rest of the domain exert some impact,
623 particularly in terms of enhancing rainfall along the equatorward margin of the SPCZ. As shown
624 in Fig. 11c, the equatorward margin of the SPCZ manifests a positive precipitation anomaly
625 associated with the column radiative forcing component of the MSE source. On the other hand,
626 over much of South America and the Atlantic, it is the total MSE forcing outside of the
627 equatorial Pacific region dominates the response. The monsoon region of northern Australia is
628 notable for having opposite-signed precipitation anomalies based on considering MSE sources
629 inside and outside of the ENSO source region.

630
631 **8. Summary and conclusions**

632 In this study, we have applied a framework developed by Boos and Korty (2016) to estimate the
633 SPCZ response to ENSO based on assumed relationships between changes in atmospheric
634 energy transport, in terms of divergent moist static energy flux, and shifts in convection zones.
635 In particular, this framework generalizes to 2D the linkage between shifts in the zonal-mean

ITCZ and the energy flux equator, the latter associated with the latitude of vanishing zonal-mean meridional moist static energy flux. The 2D energetics framework further permits diagnosis of ENSO-related SPCZ displacements in terms of component processes or mechanisms associated with ENSO, e.g., the partitioning of moist static energy transport into component dry static energy and moisture transports or surface turbulent fluxes and column radiative fluxes, as well as the spatial characteristics of the anomalous MSE sources occurring during El Niño.

The advantage of working with vertically-integrated MSE is that the precipitation does not appear explicitly in the MSE budget (unlike in either atmospheric temperature or moisture budgets separately). However, it is clear that the spatial patterns of anomalous MSE sources strongly resemble anomalous precipitation, indicative of the operation of feedbacks associated with precipitation changes, e.g., cloud-radiative or water vapor feedbacks. Although we have not done so here, such feedbacks could be isolated and their impacts quantified by analyzing the EFE/EPM changes associated with MSE feedback sources. Of course, an important caveat to is that the approach is still fundamentally diagnostic, so care should be taken in drawing inferences about causality.

While we have emphasized the ENSO response of the SPCZ region, where the 2D energetics framework appears to be especially consistent with the observations, we also noted some consistency to the observed ENSO response in rainfall over other parts of the tropics, such as northeastern South America. However, it is also possible to draw conclusions from regions where predictions of the 2D framework fail to agree with observations. For example, the 2D framework does not agree well with observed behavior over southeastern South America, but previous studies have pointed to a forced extratropical Rossby wave as the source of the observed precipitation increase over that region during El Niño events.

We suggest that the 2D energetics framework may ultimately provide a useful tool for multimodel analysis, particularly in terms of interpreting some of the problematic tropical precipitation biases models in current-generation climate models. Among these, the double ITCZ in the eastern Pacific is arguably the most well-known, but the SPCZ also manifests biases, e.g., some current generation models simulate a too zonal SPCZ and/or SPCZ rainfall extending too far to the east, particularly in coupled models (Lintner et al. 2016). Given that model biases likely involve the details of the parameterizations involved, the 2D energetics framework is unlikely to identify directly the bias sources. Nevertheless, it may provide guidance about how biases in rainfall distribution relate to other quantities, like surface or radiative fluxes, particularly when these may occur remotely.

Acknowledgments

We thank Max Pike for graphical assistance. BRL acknowledges support from National Science Foundation award AGS-1505198 and New Jersey Agricultural Experiment Station project NJ07134, and WRB acknowledges support from National Science Foundation awards AGS-1763277 and AGS-1746160.

References Cited

- Adam, O., T. Bischoff, and T. Schneider, 2016: Seasonal and interannual variations in the energy flux equator and ITCZ. Part II: Zonally varying shifts in the ITCZ. *J. Clim.*, 29, 7281–7293, doi:10.1175/JCLI-D-15-0710.1.
- Back, L. E., and C. S. Bretherton, 2006: Geographic variability in the export of moist static energy and vertical motion profiles in the tropical Pacific. *Geophys. Res. Lett.*, 33, L17810, doi:10.1029/2006GL026672.
- Bendix, A. and J. Bendix, 2006: Heavy rainfall episodes in Ecuador during El Niño events and associated regional atmospheric circulation and SST patterns. *Adv. Geosci.*, 6, 43-49, <https://doi.org/10.5194/adgeo-6-43-2006>.
- Berrisford, P., P., Kallberg, S. Kobayashi, D. Dee, S. Uppala, A. J. Simmons, P. Poli, and H. Sato, 2011: Atmospheric conservation properties in ERA-Interim. *Q. J. Roy. Meteorol. Soc.*, 137, 1381–1399, doi:10.1002/qj.864.
- Biasutti, M., A. Voigt, W. R. Boos, P. Braconnot, J. C. Hargreaves, S. P. Harrison, S. M. Kang, B. E. Mapes, J. Scheff, C. Schumacher, A. H. Sobel, and S.-P. Xie, 2018. Global energetics and local physics as drivers of past, present and future monsoons. *Nat. Geosci.*, 11, 392-400 (2018).
- Bischoff, T., and T. Schneider, 2014: Energetic constraints on the position of the intertropical convergence zone. *J. Clim.*, 27, 4937–4951, doi: 10.1175/JCLI-D-13-00650.1.
- Boos, W. R., and R. L. Korty, 2016: Regional energy budget control of the intertropical convergence zone and application to mid-Holocene rainfall. *Nature Geosci.*, 9, 892–897, doi:10.1038/ngeo2833.
- Borlace, S., A. Santoso, W. Cai, and M. Collins, 2014: Extreme swings of the South Pacific Convergence Zone and the different types of El Niño events. *Geophys. Res. Lett.*, doi:10.1002/2014GL060551.
- Broccoli, A. J., K. A. Dahl, and R. J. Stouffer, 2006: Response of the ITCZ to Northern Hemisphere cooling. *Geophys. Res. Lett.*, 33, L01702, doi:10.1029/2005GL024546.
- Capotondi A., A. T. Wittenberg, M. Newman, E. Di Lorenzo, J.-Y. Yu, and co-authors, 2015: Understanding ENSO diversity. *Bull. Amer. Meteor. Soc.*, 96, 921-938, doi:10.1175/BAMS-D-13-00117.1.
- Carvalho, L. M. V., C. Jones, and B. Liebmann, 2004: The South Atlantic convergence zone: Intensity, form, persistence, and relationships with intraseasonal to interannual activity and extreme rainfall. *J. Clim.*, 17, 88–108, doi:10.1175/1520-0442(2004)017<0088:TSACZI>2.0.CO;2.

- Chiang, J. C. H., and C. M. Bitz, 2005: Influence of high latitude ice cover on the marine Intertropical Convergence Zone. *Clim. Dyn.*, 25, 477–496.
- Chiang, J. C. H., and B. R. Lintner, 2005: Mechanisms of remote tropical surface warming during El Niño. *J. Clim.*, 18, 4130 – 4149, doi: 10.1175/JCLI3529.1.
- Choi, K.-Y., G. A. Vecchi, and A. T. Wittenberg, 2015: Nonlinear zonal wind response to ENSO in the CMIP5 models: Roles of the zonal and meridional shift of the ITCZ/SPCZ and the simulated climatological precipitation. *J. Clim.*, 28, 8556–8573, doi:10.1175/JCLI-D-15-0211.1.
- Chou, C., and M.-H. Lo, 2007: Asymmetric responses of tropical precipitation during ENSO. *J. Clim.*, 19, 3411–3433, doi: 10.1175/JCLI4197.1.
- Clem K., and J. Renwick, 2015: Austral Spring Southern hemisphere circulation and temperature changes and links to the SPCZ. *J. Clim.*, 28, 7371–84.
- Colasacco-Thumm, N., 2015: An Investigation of Surface Heat Fluxes During El Niño-Southern Oscillation (ENSO) Evolution in Reanalyses. M.S. Thesis, Department of Atmospheric and Oceanic Sciences, University of Wisconsin-Madison, 70 pp.
- Dee, D. P., Uppala, S. M., Simmons, A. J., Berrisford, P., Poli, P., Kobayashi, S., Andrae, U., Balmaseda, M. A., Balsamo, G., Bauer, P., Bechtold, P., Beljaars, A. C. M., van de Berg, L., Bidlot, J., Bormann, N., Delsol, C., Dragani, R., Fuentes, M., Geer, A. J., Haimberger, L., Healy, S. B., Hersbach, H., Hólm, E. V., Isaksen, I., Kållberg, P., Köhler, M., Matricardi, M., McNally, A. P., Monge-Sanz, B. M., Morcrette, J.-J., Park, B.-K., Peubey, C., de Rosnay, P., Tavolato, C., J.-N. Thépaut and F. Vitart, 2011: The ERA-Interim reanalysis: configuration and performance of the data assimilation system. *Q.J.R. Meteorol. Soc.*, 137: 553–597. doi: 10.1002/qj.828
- Donohoe, A., J. Marshall, D. Ferreira, and D. McGee, 2013: The relationship between ITCZ location and cross-equatorial atmospheric heat transport: From the seasonal cycle to the last glacial maximum. *J. Clim.*, 26, 3597–3618, doi: 10.1175/JCLI-D-12-00467.1.
- Fairall, C. W., E. F. Bradley, D. P. Rogers, J. B. Edson, and G. S. Young, 1996: Bulk parameterization of air-sea fluxes for Tropical Ocean-Global Atmosphere Coupled-Ocean Atmosphere Response Experiment. *J. Geophys. Res.*, 101(C2), 3747–3764, doi:10.1029/95JC03205.
- Folland, C. K., J. A. Renwick, M. J. Salinger, and A. B. Mullan, 2002: Relative influences of the Interdecadal Pacific Oscillation and ENSO on the South Pacific Convergence Zone. *Geophys. Res. Lett.*, 29, doi:10.1029/2001GL014201.
- Green, B., and J. Marshall, 2017: Coupling of trade winds with ocean circulation damps ITCZ shifts. *J. Clim.*, 30, 4395–4411, doi:10.1175/JCLI-D-16-0818.1.
- Grimm, A. M., and R. G. Tedeschi, 2009: ENSO and extreme rainfall events in South America. *J. Clim.*, 22, 1589–1609, doi:10.1175/2008JCLI2429.1.

- Haffke, C. and G. Magnúsdóttir, 2013: The South Pacific Convergence Zone in three decades of satellite images. *J. Geophys. Res. Atmos.*, *118*, 10839–10849, doi:10.1002/jgrd.50838.
- Juillet-Leclerc, A., S. Thiria, P. Naveau, T. Delcroix, N. Le Bec, D. Blamart, and T. Corrège, 2006: SPCZ migration and ENSO events during the 20th century as revealed by climate proxies from a Fiji coral. *Geophys. Res. Lett.*, *33*, L17710, doi:10.1029/2006GL025950.
- Kang, S. M., I. M. Held, D. M. W. Frierson, and M. Zhao, 2008: The Response of the ITCZ to extratropical thermal forcing: Idealized slab-ocean experiments with a GCM. *J. Clim.*, *21*, 3521–3532, doi: 10.1175/2007JCLI2146.1.
- Kang, S. M., Y. Shin and S.-P. Xie, 2018: Extratropical forcing and tropical rainfall distribution : energetics framework and ocean Ekman advection. *Clim. Atmos. Sci.*, *2*, doi:10.1038/s41612-017-0046-6.
- Kao, H. Y., and J. Y. Yu, 2009: Contrasting eastern Pacific and central Pacific types of ENSO. *J. Clim.*, *22*, 615–632, doi:10.1175/2008JCLI2309.1.
- Kidwell, A., T. Lee, Y.-H. Jo, and X.-H. Yan, 2016: Characterization of the variability of the South Pacific Convergence Zone using satellite and reanalysis wind products. *J. Clim.*, *29*, 1717–1732, doi: 10.1175/JCLI-D-15-0536.1.
- Kubar, T. L., D. L. Hartmann, and R. Wood, 2007: Radiative and Convective Driving of Tropical High Clouds. *J. Clim.*, *20*, 5510–5526, doi:10.1175/2007JCLI1628.1.
- L'Ecuyer, T. S., and G. L. Stephens, 2007: The Tropical Atmospheric Energy Budget from the TRMM Perspective. Part II: Evaluating GCM Representations of the Sensitivity of Regional Energy and Water Cycles to the 1998-99 ENSO Cycle. *J. Clim.*, *20*, 4548–4571, doi: 10.1175/JCLI4207.1.
- Lintner, B. R., and J. D. Neelin, 2008: Eastern margin variability of the South Pacific Convergence Zone. *Geophys. Res. Lett.*, *35*, L16701, doi:10.1029/2008GL034298.
- Lintner, B. R., B. Langenbrunner, J. D. Neelin, B. T. Anderson, M. J. Niznik, G. Li, and S.-P. Xie, 2016: Characterizing CMIP5 model spread in simulated rainfall in the Pacific intertropical convergence and South Pacific convergence zones. *J. Geophys. Res. Atmos.*, *121*, 11,590–11,607, doi:10.1002/2016JD025284.
- Lorrey A., G. Dalu, J. Renwick, H. Diamond, and M. Gaetani, 2012: Reconstructing the South Pacific convergence zone position during the presatellite era: a La Niña case study. *Mon. Weather Rev.*, *140*, 3653–3668. doi:10.1175/MWR-D-11-00228.1
- Matthews, A. J., B. J. Hoskins, J. M. Slingo, and M. Blackburn, 1996: Development of convection along the SPCZ within a Madden-Julian oscillation. *Q. J. Roy. Meteor. Soc.*, *122*, 669–688.

- Matthews, A. J., 2012: A multiscale framework for the origin and variability of the South Pacific Convergence Zone. *Q. J. Roy. Meteor. Soc.*, *138*, 1165–1178, doi: 10.1002/qj.1870.
- Mayer, M., K. E. Trenberth, L. Haimberger, and J. T. Fasullo, 2013: The response of tropical atmospheric energy budgets to ENSO. *J. Clim.* *26*, 4710–4724, doi: 10.1175/JCLI-D-12-00681.1.
- Mayer, M., L. Haimberger, and M. A. Balmaseda, 2014: On the energy exchange between tropical ocean basins related to ENSO. *J. Clim.* *27*, 6393–6403, doi: 10.1175/JCLI-D-14-00123.1.
- McGee, D., A. Donohoe, J. Marshall, and D. Ferreira, 2014: Changes in ITCZ location and cross-equatorial heat transport at the Last Glacial Maximum, Heinrich Stadial 1, and the mid-Holocene. *Earth Planet. Sci. Lett.*, *390*, 69–79, doi: 10.1016/j.epsl.2013.12.043.
- Murphy, B., S. B. Power, and S. McGree, 2014: The varied impacts of El Niño - Southern Oscillation on Pacific island climate. *J. Clim.*, *27*, 4015–4036, doi: 10.1175/JCLI-D-13-00130.1.
- Neelin, J. D., and I. M. Held, 1987: Modeling tropical convergence based on the moist static energy budget. *Mon. Wea. Rev.*, *115*, 3–12.
- Neelin, J. D., C. Chou, and H. Su, 2003: Tropical drought regions in global warming and El Niño teleconnections, *Geophys. Res. Lett.*, *30*(24), 2275, doi:10.1029/2003GL018625.
- Neelin, J. D., 2007: Moist dynamics of tropical convection zones in monsoons, teleconnections and global warming. In *The Global Circulation of the Atmosphere*, T. Schneider and A. Sobel, Eds, Princeton University Press, Princeton, 385pp.
- Niznik, M. J. and B. R. Lintner, 2013: Circulation, Moisture, and Precipitation Relationships along the South Pacific Convergence Zone in Reanalyses and CMIP5 models. *J. Clim.*, *26*, 10174–10192, doi:10.1175/JCLI-D-13-00263.1.
- Niznik, M. J., B. R. Lintner, A. J. Matthews, and M. J. Widlansky, 2015: The role of tropical-extratropical interaction and synoptic variability in maintaining the South Pacific Convergence Zone in CMIP5 models. *J. Clim.*, *28*, 3353–3374, doi:10.1175/JCLI-D-14-00527.1.
- Paek, H., J.-Y. Yu, and C. Qian, 2017: Why were the 2015/2016 and 1997/1998 extreme El Niños different?, *Geophys. Res. Lett.*, *44*, 1848–1856, doi:10.1002/2016GL071515.
- Peters, M. E., Z. Kuang, and C. C. Walker, 2008: Analysis of Atmospheric Energy Transport in ERA-40 and Implications for Simple Models of the Mean Tropical Circulation. *J. Clim.*, *21*, 5229–5241, doi:10.1175/2008JCLI2073.1.
- Raymond, D. J., S. Sessions, A. H. Sobel, and Z. Fuchs, 2009: The mechanics of gross moist stability. *J. Adv. Model. Earth Sys.*, *1*, doi:10.3894/JAMES.2009.1.9

- Salinger, M. J., S. McGree, F. Beucher, S. B. Power, and F. Delage, 2014: A new index for variations in the position of the South Pacific convergence zone 1910/11–2011/2012. *Clim. Dyn.*, *43*, doi:10.1007/s00382-013-2035-y.
- Schneider, T., 2017: Feedback of Atmosphere - Ocean Coupling on Shifts of the Intertropical Convergence Zone. *Geophys. Res. Lett.*, *44*, 11,644–11,653, doi: 10.1002/2017GL075817.
- Su, H., and J. D. Neelin, 2002: Teleconnection mechanisms for tropical Pacific descent anomalies during El Niño. *J. Atmos. Sci.*, *59*, 2694 – 2712, doi: 10.1175/1520-0469(2002)059<2694:TMFTPD>2.0.CO;2.
- Takahashi, K. and D.S. Battisti, 2007: Processes Controlling the Mean Tropical Pacific Precipitation Pattern. Part II: The SPCZ and the Southeast Pacific Dry Zone. *J. Clim.*, *20*, 5696–5706, <https://doi.org/10.1175/2007JCLI1656.1>.
- Trenberth, K. E., 1976: Spatial and temporal variations of the southern oscillation. *Q. J. Roy. Meteor. Soc.*, *102*, 639–653.
- Trenberth, K. E., 1997: Using atmospheric budgets as a constraint on surface fluxes. *J. Clim.*, *10*, 2796–2809.
- Trenberth, K. E., J. M. Caron, and D. P. Stepaniak, 2001: The atmospheric energy budget and implications for surface fluxes and ocean heat transports. *Clim. Dyn.*, *17*, 259–276.
- van der Wiel, K., A. J. Matthews, D. P. Stevens, and M. M. Joshi, 2015: A dynamical framework for the origin of the diagonal South Pacific and South Atlantic Convergence Zones. *Q. J. Roy. Meteor. Soc.*, *141*, 1997–2010. doi:10.1002/qj.2508
- Vincent, D. G., 1994: The South Pacific Convergence Zone (SPCZ): A Review. *Mon. Wea. Rev.*, *122*, 1949–1970, [https://doi.org/10.1175/1520-0493\(1994\)122<1949:TSPCZA>2.0.CO;2](https://doi.org/10.1175/1520-0493(1994)122<1949:TSPCZA>2.0.CO;2).
- Vincent, E. M., M. Lengaigne, C. E. Menkes, N. C. Jourdain, P. Marchesiello, and G. Madec, 2011: Interannual variability of the South Pacific Convergence Zone and implications for tropical cyclone genesis. *Climate Dyn.*, *36*, 1881–1896, doi:10.1007/s00382-009-0716-3.
- Wang, B., and T. Li, 1993: A simple tropical atmospheric model of relevance to short-term climate variation. *J. Atmos. Sci.*, *50*, 260–284.
- Widlansky, M. J., P. J. Webster, and C. D. Hoyos, 2011: On the location and orientation of the South Pacific Convergence Zone. *Climate Dyn.*, *36*, 561–578, doi:10.1007/s00382-010-0871-6.
- Xie, P. and P. A. Arkin, 1997: Global precipitation: A 17-year monthly analysis based on gauge observations, satellite estimates, and numerical model outputs. *Bull. Amer. Meteor. Soc.*, *78*, 2539–2558.

905 Yeh, S.-W., W. Cai, S.-K. Min, M. J. McPhaden, D. Dommenges, B. Dewitte, M. Collins, K.
906 Ashok, S.-I. An, B.-Y. Yim, and J.-S. Kug, 2018: ENSO atmospheric teleconnections and their
907 response to greenhouse gas forcing. *Rev. Geophys*, 56, 185–206.
908 <https://doi.org/10.1002/2017RG000568>.
909

Table and Figure Captions

Table 1: CPC classifications of DJFs by ENSO phase. Years indicated correspond to January, e.g., 1980 is December 1979-February 1980. Strong El Niño DJFs, with ONI values above 2°C, are indicated in bold.

Fig. 1: SPCZ region precipitation climatology from CMAP (line contours; in units of mm day⁻¹) and precipitation composite difference for El Niño minus La Niña conditions (shading; in mm day⁻¹) for DJF. Stippling indicates gridpoints for which the differences are significant at the 99% level according to Welch's t-test. The black line denotes the cross-SPCZ transect along which precipitation is sampled in subsequent figures.

Fig. 2: ENSO variability along the SPCZ transect. a) Standardized anomalies of ONI (black), maximum precipitation rate along the transect (green), and location of the maximum precipitation (orange). For the latter, positive (negative) anomalies correspond to a more northeastward (southwestward) location. b) Composites of along-transect precipitation (solid lines) for ENSO neutral years (gray), El Niño years (red), and La Niña years (blue). Also shown is the composite of precipitation for the three strongest El Niño events, 1983, 1998, and 2016 (red line with squares). Dashed red and blue lines correspond to shifts of the neutral condition composites that best approximate, respectively, the El Niño and La Niña phase composites.

Fig. 3: ENSO neutral condition precipitation (shading; in mm day⁻¹), MSE flux potential (line contours; contouring interval is 0.2 PW, with the zero contour omitted), and divergent MSE flux. Also shown are the locations of the energy flux equator and energy flux prime meridians for neutral conditions.

Fig. 4: Observed El Niño minus La Niña condition composite differences of precipitation (shading; in mm day⁻¹), MSE flux potential difference for El Niño minus La Niña phase conditions (line contours; contouring interval is 0.04 PW, with the zero contour omitted), and the anomalous divergent MSE flux (arrows). Also shown are the locations of the energy flux equator and energy flux prime meridians for El Niño and La Niña phase conditions (red and blue contours, respectively).

Fig. 5: a) El Niño (theory) minus La Niña (observed) condition composite precipitation difference (shading; in mm day⁻¹), based on the analyzed MSE flux. For reference, the 4 mm day⁻¹ contour for neutral conditions is included. b) Observed El Niño and La Niña cross-SPCZ transects (red and blue, respectively) and theoretical estimate for El Niño (dashed).

Fig. 6: Observed precipitation (solid lines) and estimated meridional component of the divergent MSE flux (x symbols) for El Niño and La Niña conditions (red and blue, respectively) at 140° W. Also shown is the El Niño profile from theory (dashed red line).

Fig. 7: MSE sources (shading), MSE flux divergent potential (contours), and divergent flux components (arrows) for the toy model of the SPCZ shift in response to ENSO. The red region corresponds to the mean state MSE source and the blue region to the perturbation source associated with El Niño conditions, with purple denoting the overlap of the mean and

perturbation MSE sources. The solid gray line is the mean state EFE, while the dashed line is the EFE during El Niño conditions.

Fig. 8: Latitude of the EFE (blue symbols) and the flux potential ridge (red symbols) as a function of the anomalous MSE source at 160°W. Here the anomalous MSE source has been normalized by the mean state MSE source ($F_0 = 1$).

Fig. 9: a) As in Fig. 4, but with the flux potential computed assuming only the perturbation in DSE. b) As in Fig. 4, but with the flux potential computed assuming only the perturbation in latent heating.

Fig. 10: El Niño minus La Niña condition composite differences of: a) the total MSE source, Q_{tot} (shading; in units of $W\ m^{-2}$); b) the surface turbulent flux component, Q_{surf} ; and c) the column radiative flux component, Q_{rad} . In each panel, line contours depict the MSE source for La Niña phase conditions, with a contour interval of $25\ W\ m^{-2}$ and with solid (dashed) contours corresponding to positive (negative) values. Contours greater (less) than or equal to $150\ W\ m^{-2}$ ($-150\ W\ m^{-2}$) are highlighted in red (blue) for emphasis.

Fig. 11: El Niño (theory) minus La Nina condition composite precipitation differences, as in Figure 5a, but computed for: a) Q_{tot} ; b) Q_{surf} only; and c) Q_{rad} only.

Fig. 12: El Niño (theory) minus La Nina condition composite precipitation differences, as in Figure 5a, but for: a) MSE sources confined to the ENSO source region area only (the area within the green box); and b) MSE sources outside of the green box.

980 **Table 1:** CPC classifications of DJFs by ENSO phase. Years indicated correspond to January,
 981 e.g., 1980 is December 1979-February 1980. Strong El Niño DJFs, with ONI values above 2°C,
 982 are indicated in bold.
 983

Phase (Number of DJFs)	DJF Years
El Niño (13)	1980, 1983 , 1987, 1988, 1992, 1995, 1998 , 2003, 2005, 2007, 2010, 2015, 2016
Neutral (12)	1981, 1982, 1986, 1990, 1991, 1993, 1994, 1997, 2002, 2004, 2013, 2014
La Niña (12)	1984, 1985, 1989, 1996, 1999, 2000, 2001, 2006, 2008, 2009, 2011, 2012

984
 985

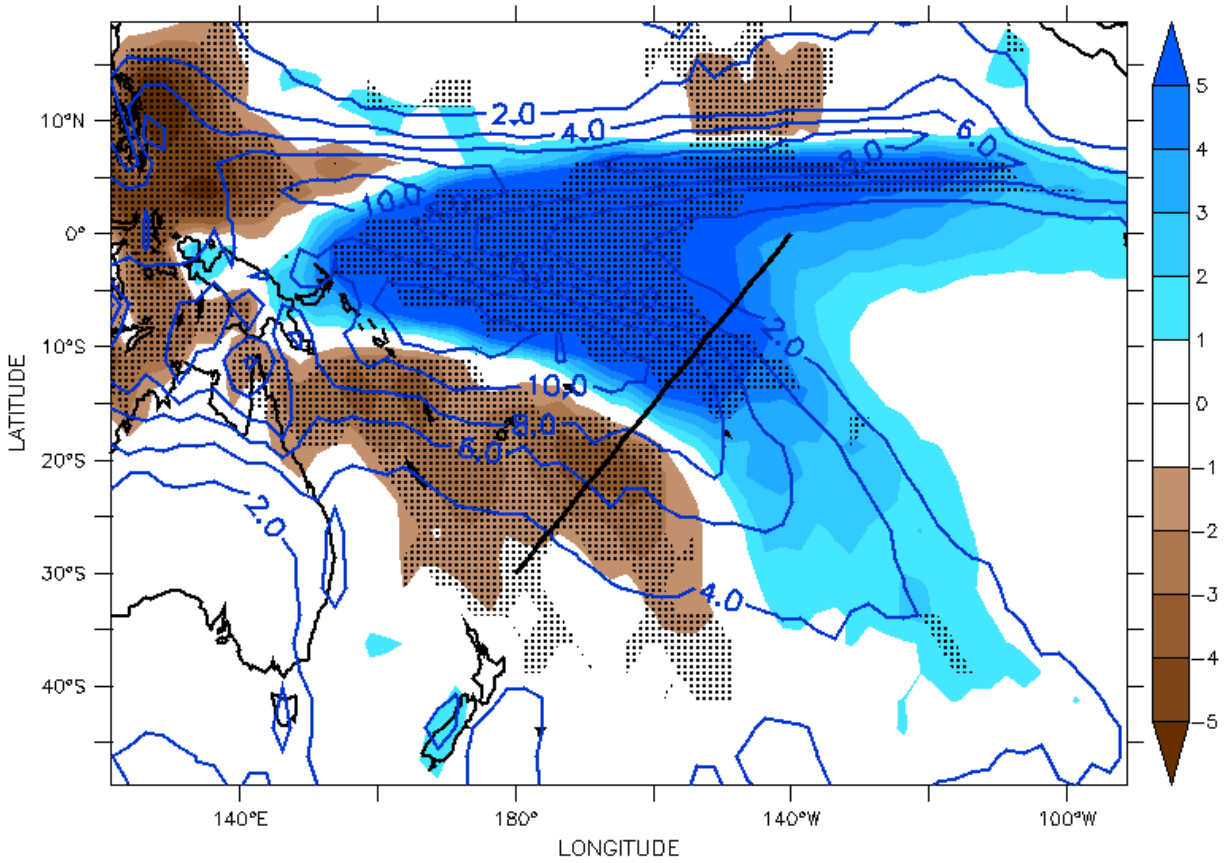


Fig. 1: SPCZ region precipitation climatology from CMAP (line contours; in units of mm day⁻¹) and precipitation composite difference for El Niño minus La Niña conditions (shading; in mm day⁻¹) for DJF. Stippling indicates gridpoints for which the differences are significant at the 99% level according to Welch's t-test. The black line denotes the cross-SPCZ transect along which precipitation is sampled in subsequent figures.

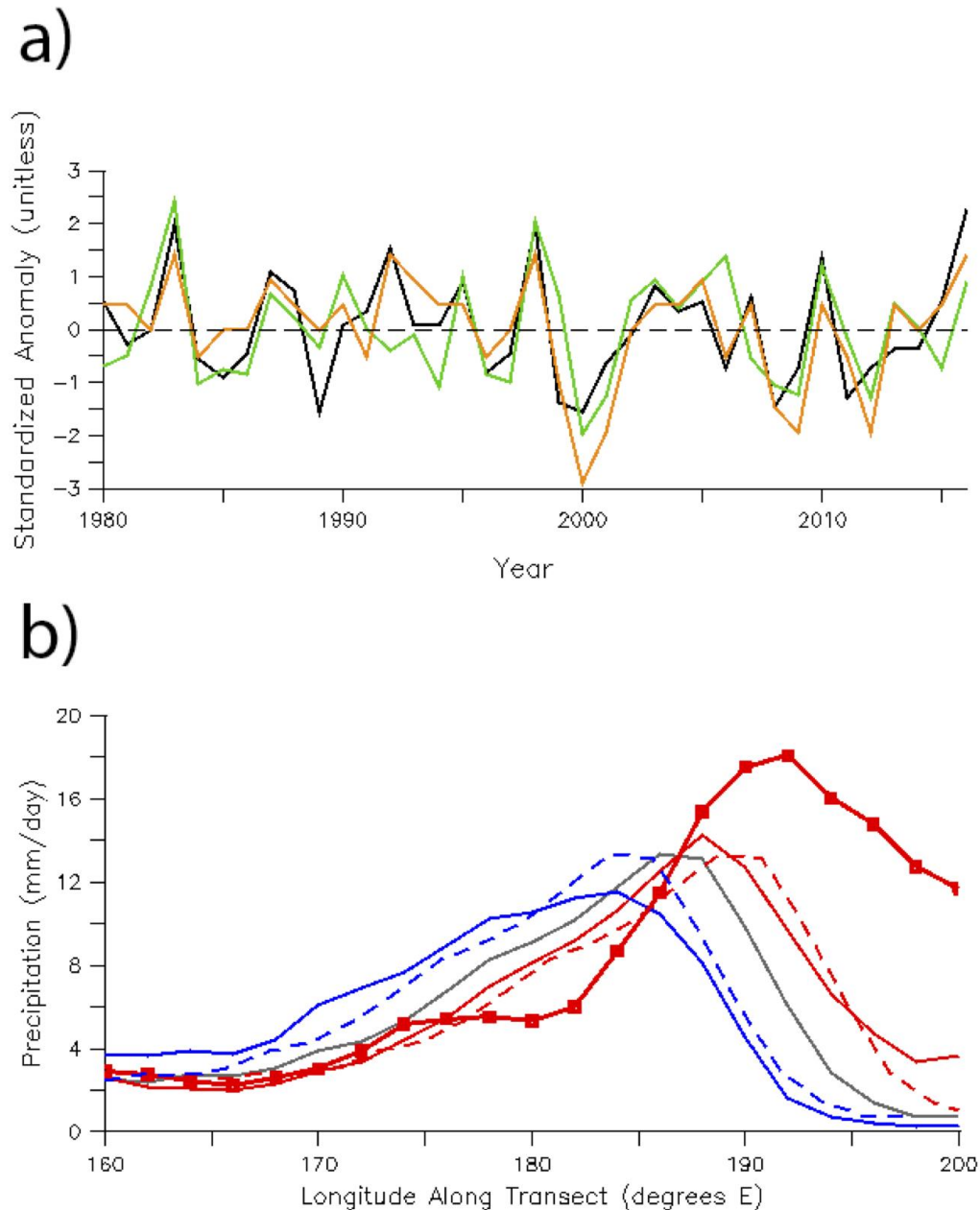


Fig. 2: ENSO variability along the SPCZ transect. a) Standardized anomalies of ONI (black), maximum precipitation rate along the transect (green), and location of the maximum precipitation (orange). For the latter, positive (negative) anomalies correspond to a more northeastward (southwestward) location. b) Composites of along-transect precipitation (solid lines) for ENSO neutral years (gray), El Niño years (red), and La Niña years (blue). Also shown is the composite of precipitation for the three strongest El Niño events, 1983, 1998, and 2016 (red line with squares). Dashed red and blue lines correspond to shifts of the neutral condition composites that best approximate, respectively, the El Niño and La Niña phase composites.

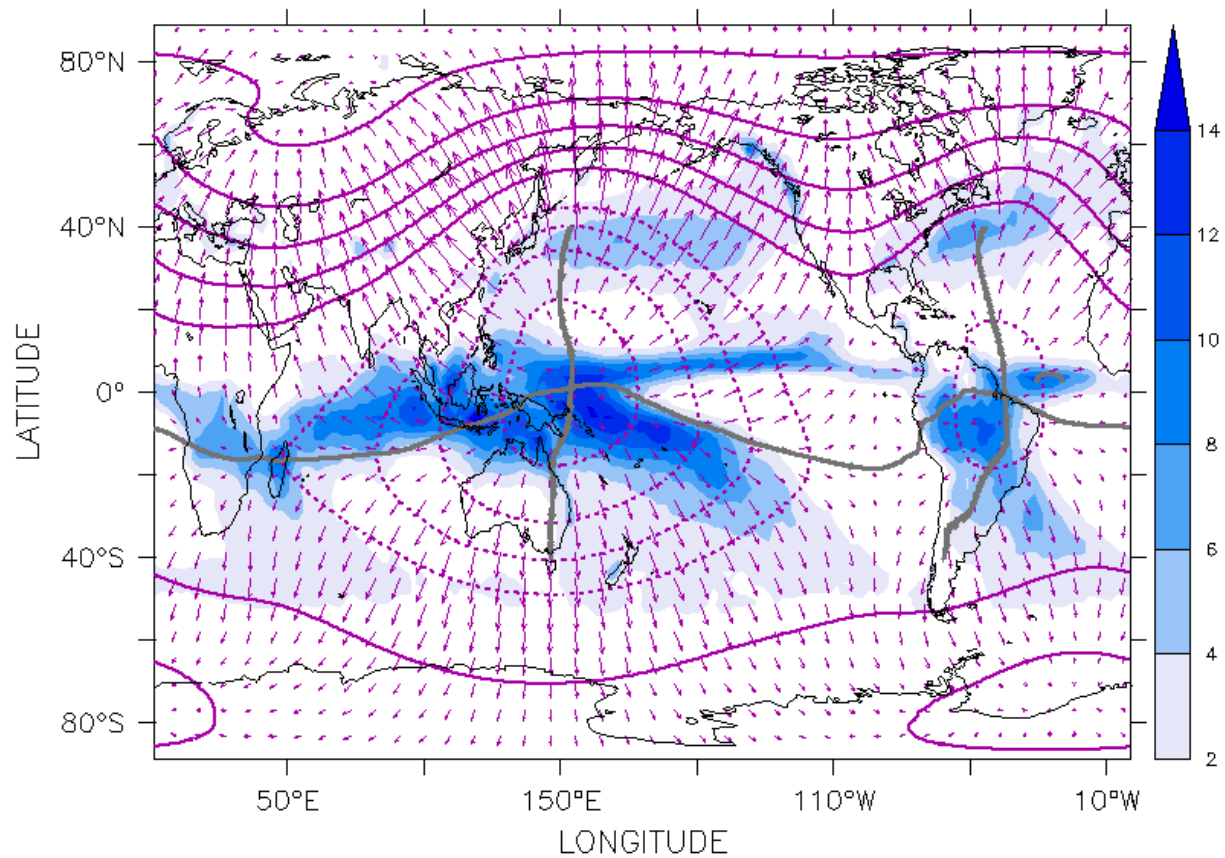


Fig. 3: ENSO neutral condition precipitation (shading; in mm day⁻¹), MSE flux potential (line contours; contouring interval is 0.2 PW, with the zero contour omitted), and divergent MSE flux. Also shown are the locations of the energy flux equator and energy flux prime meridians for neutral conditions.

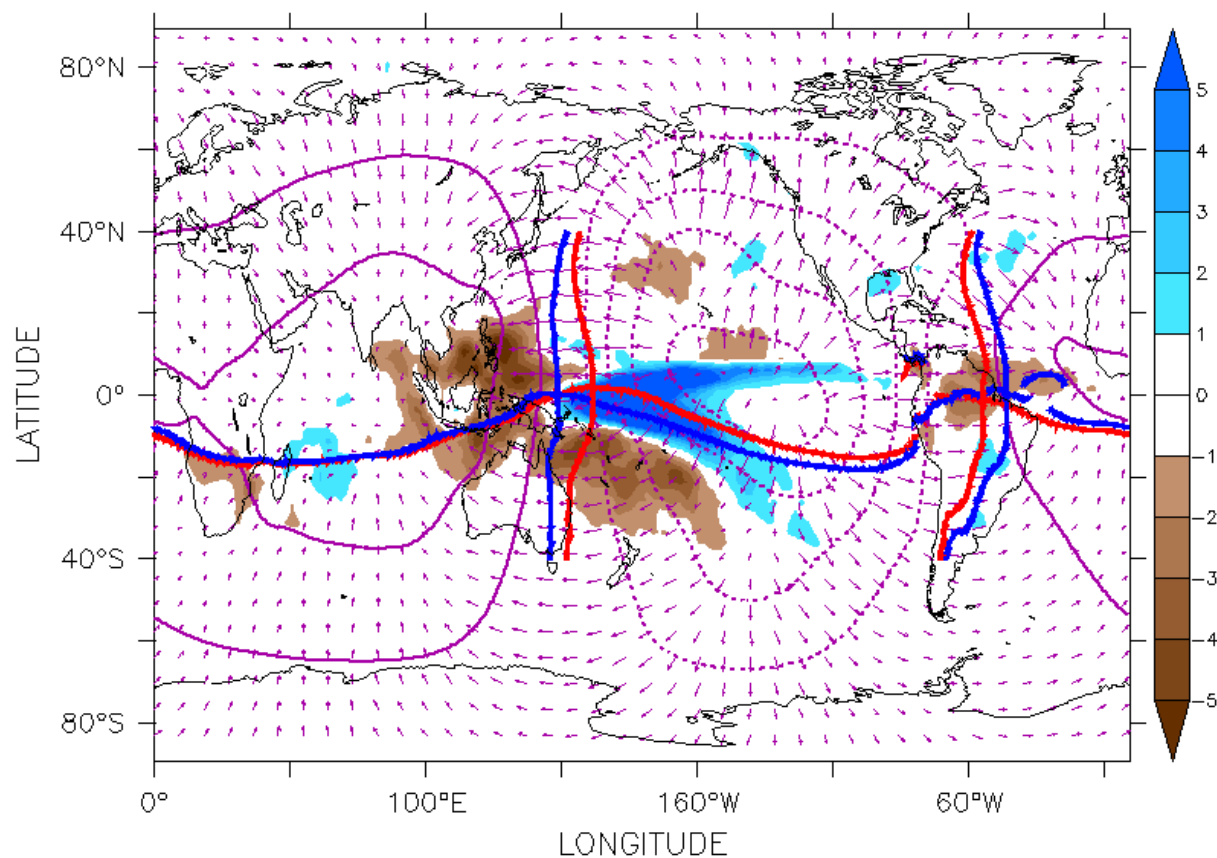
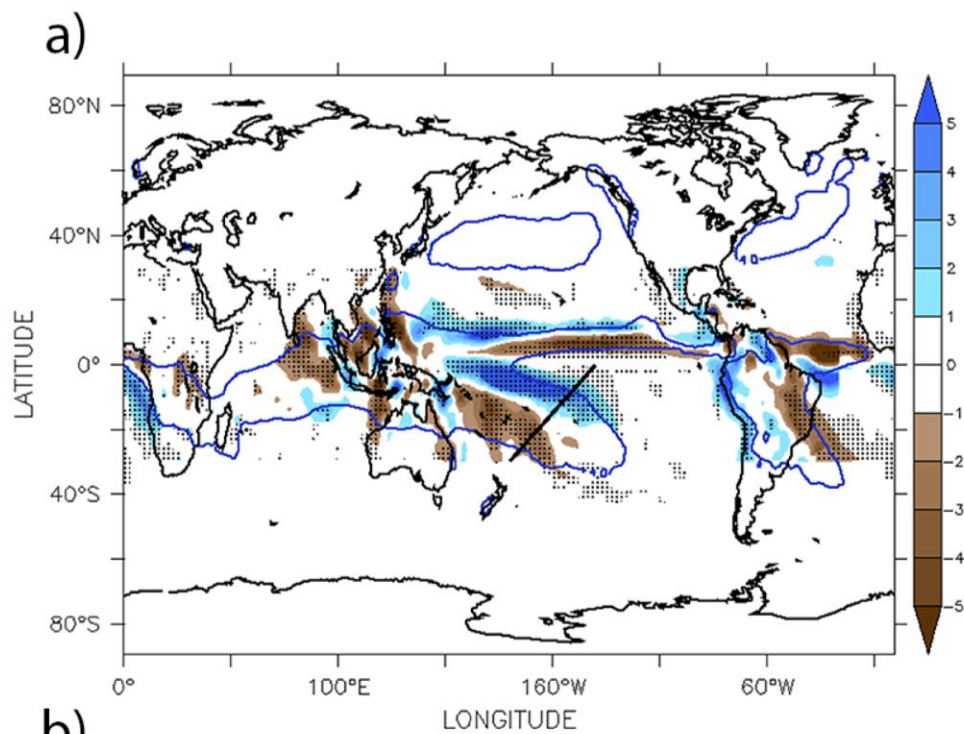


Fig. 4: Observed El Niño minus La Niña condition composite differences of precipitation (shading; in mm day^{-1}), MSE flux potential difference for El Niño minus La Niña phase conditions (line contours; contouring interval is 0.04 PW, with the zero contour omitted), and the anomalous divergent MSE flux (arrows). Also shown are the locations of the energy flux equator and energy flux prime meridians for El Niño and La Niña phase conditions (red and blue contours, respectively).



b)

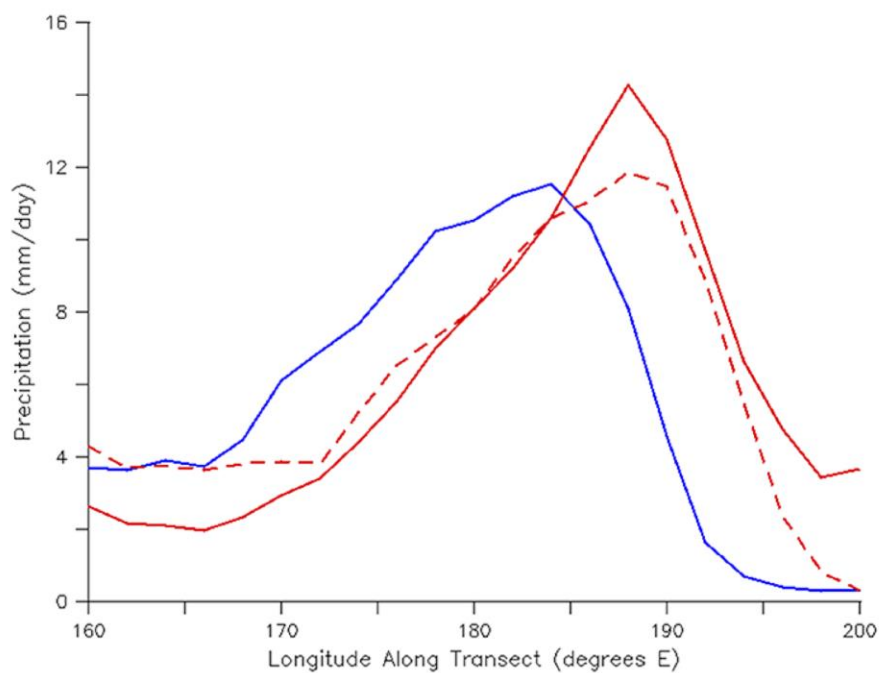


Fig. 5: a) El Niño (theory) minus La Nina (observed) condition composite precipitation difference (shading; in mm day^{-1}), based on the analyzed MSE flux. For reference, the 4 mm day^{-1} contour for neutral conditions is included. b) Observed El Niño and La Nina cross-SPCZ transects (red and blue, respectively) and theoretical estimate for El Niño (dashed).

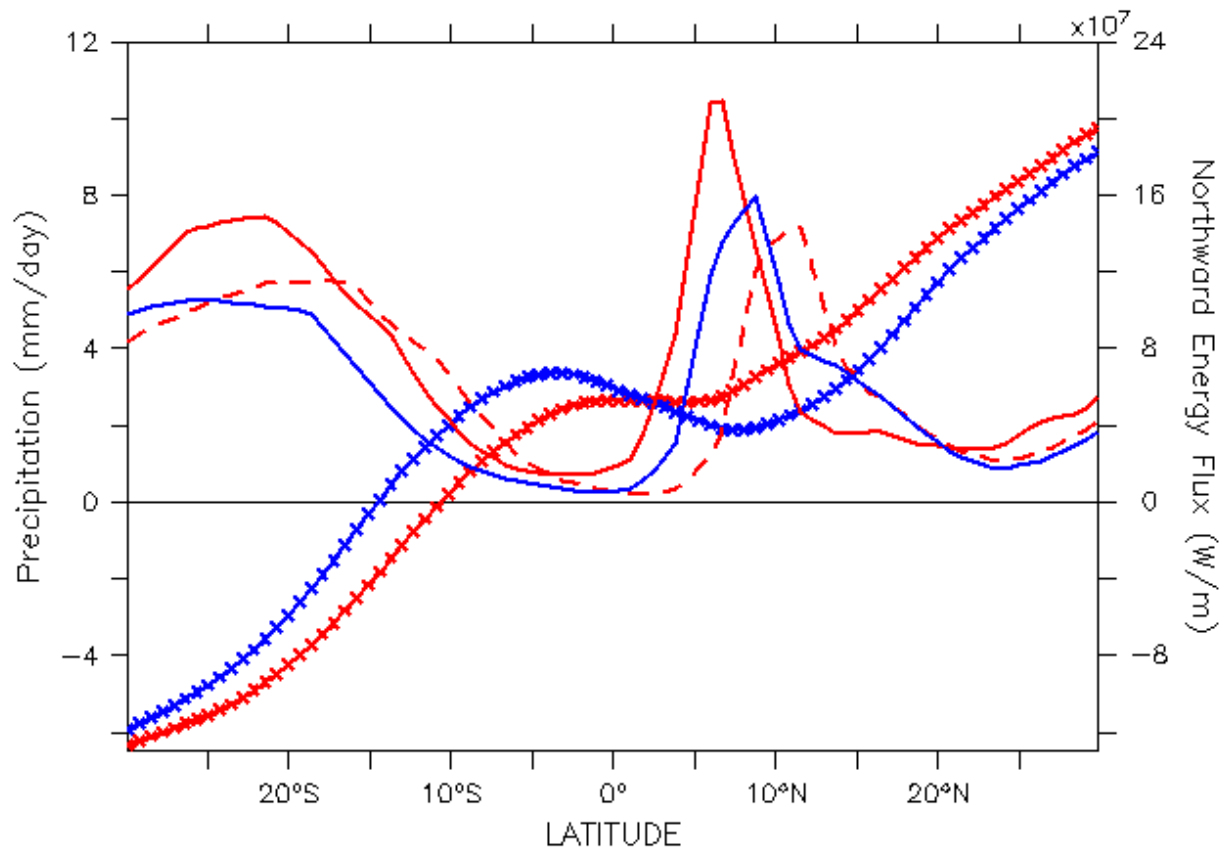


Fig. 6: Observed precipitation (solid lines) and estimated meridional component of the divergent MSE flux (x symbols) for El Niño and La Niña conditions (red and blue, respectively) at 140° W. Also shown is the El Niño profile from theory (dashed red line).

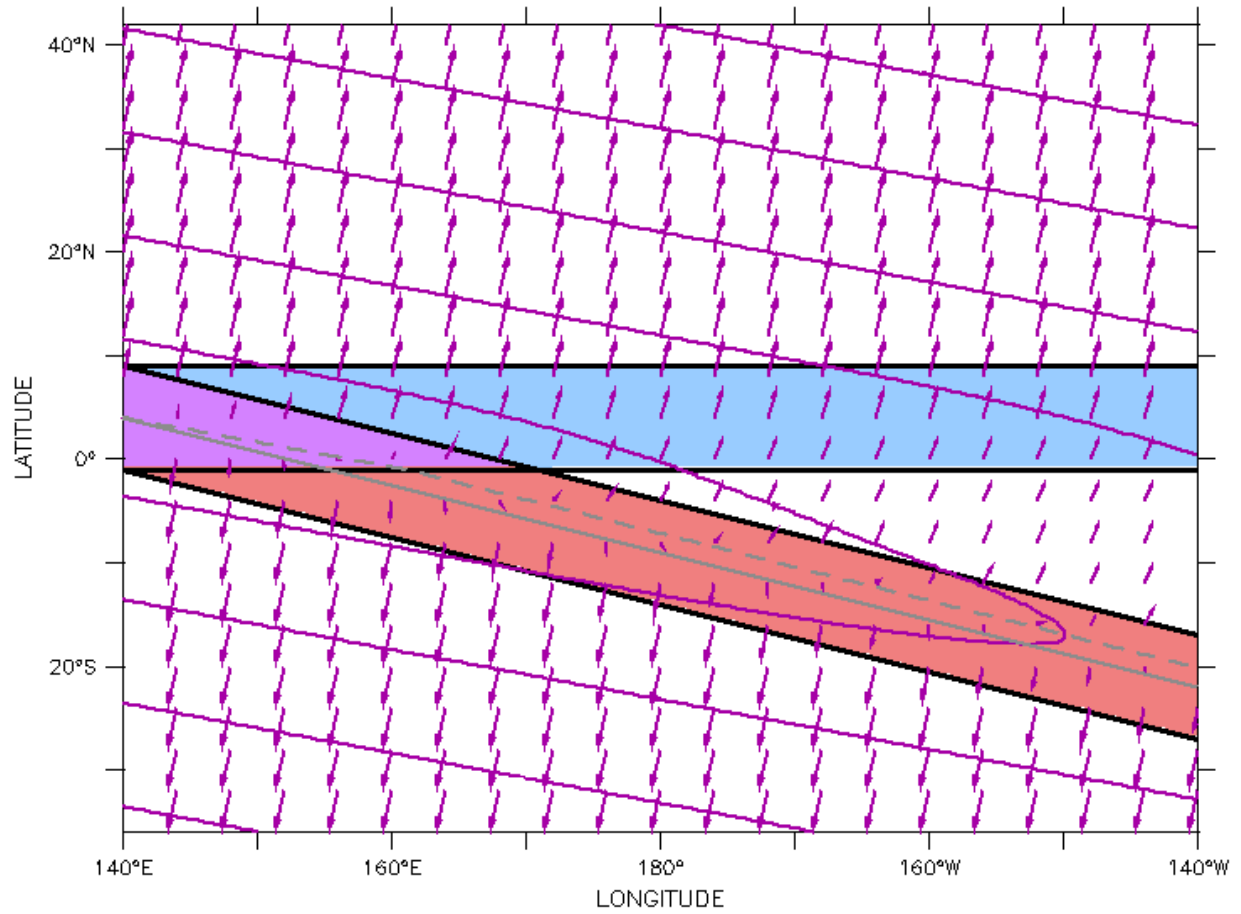


Fig. 7: MSE sources (shading), MSE flux divergent potential (contours), and divergent flux components (arrows) for the toy model of the SPCZ shift in response to ENSO. The red region corresponds to the mean state MSE source and the blue region to the perturbation source associated with El Niño conditions, with purple denoting the overlap of the mean and perturbation MSE sources. The solid gray line is the mean state EFE, while the dashed line is the EFE during El Niño conditions.

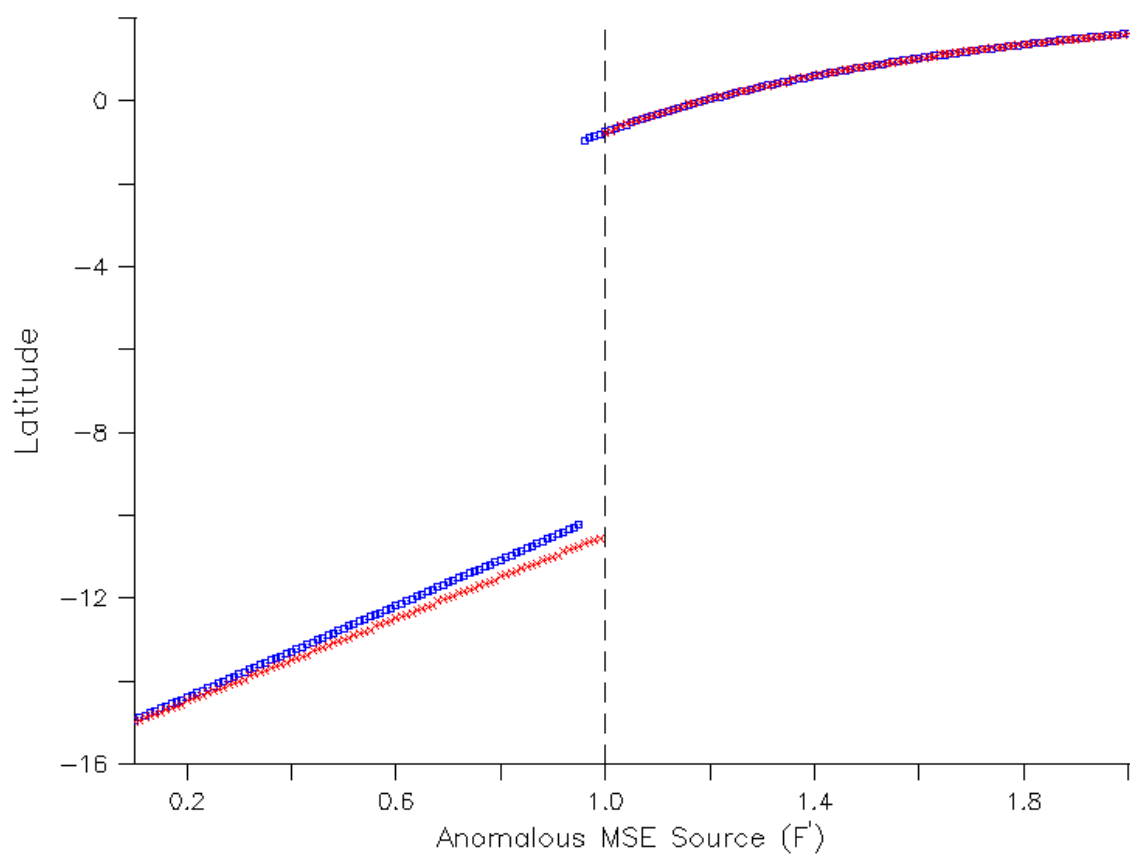


Fig. 8: Latitude of the EFE (blue symbols) and the flux potential ridge (red symbols) as a function of the anomalous MSE source at 160°W . Here the anomalous MSE source has been normalized by the mean state MSE source ($F_0 = 1$).

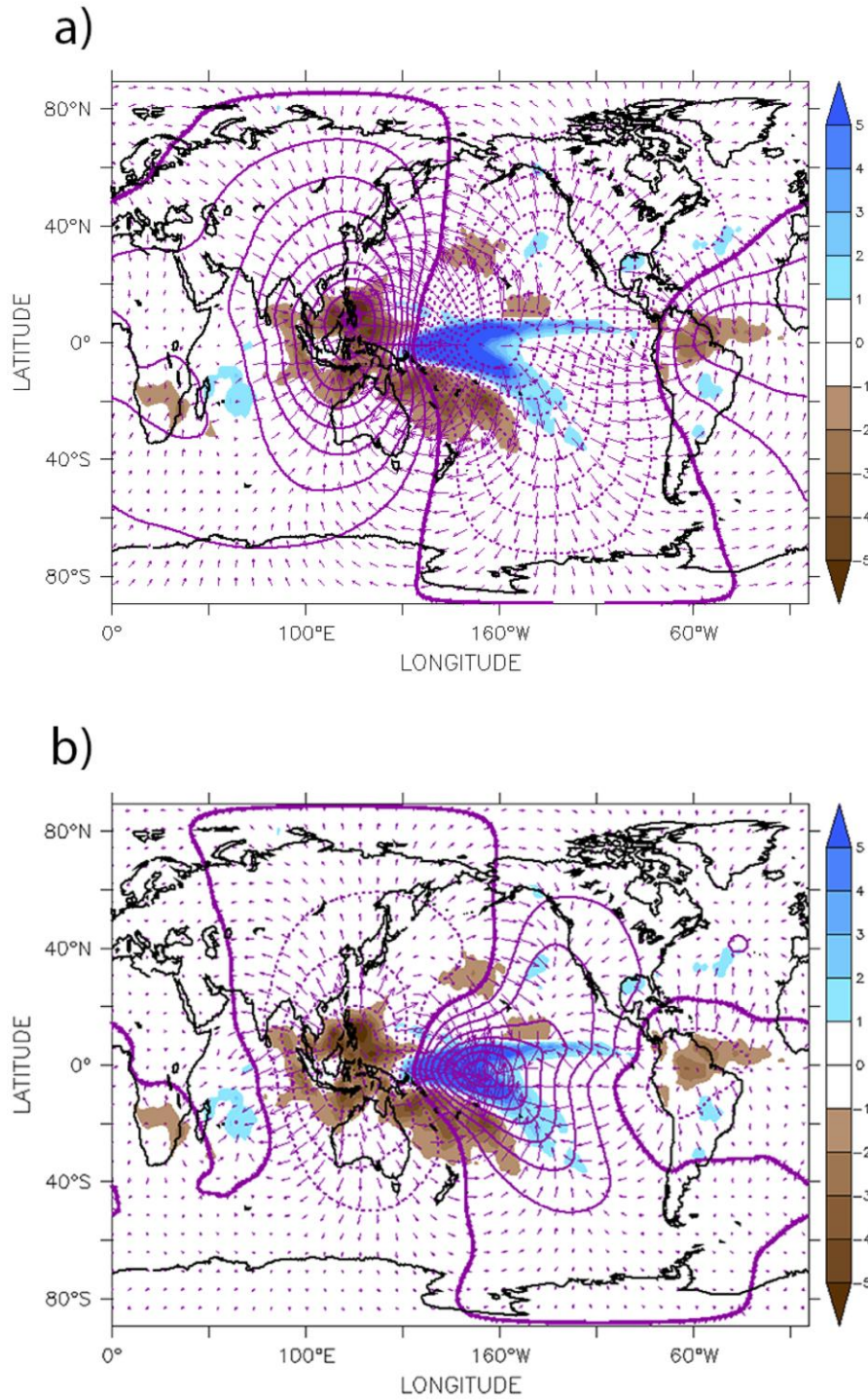


Fig. 9: a) As in Fig. 4, but with the flux potential computed assuming only the perturbation in DSE. b) As in Fig. 4, but with the flux potential computed assuming only the perturbation in latent heating.

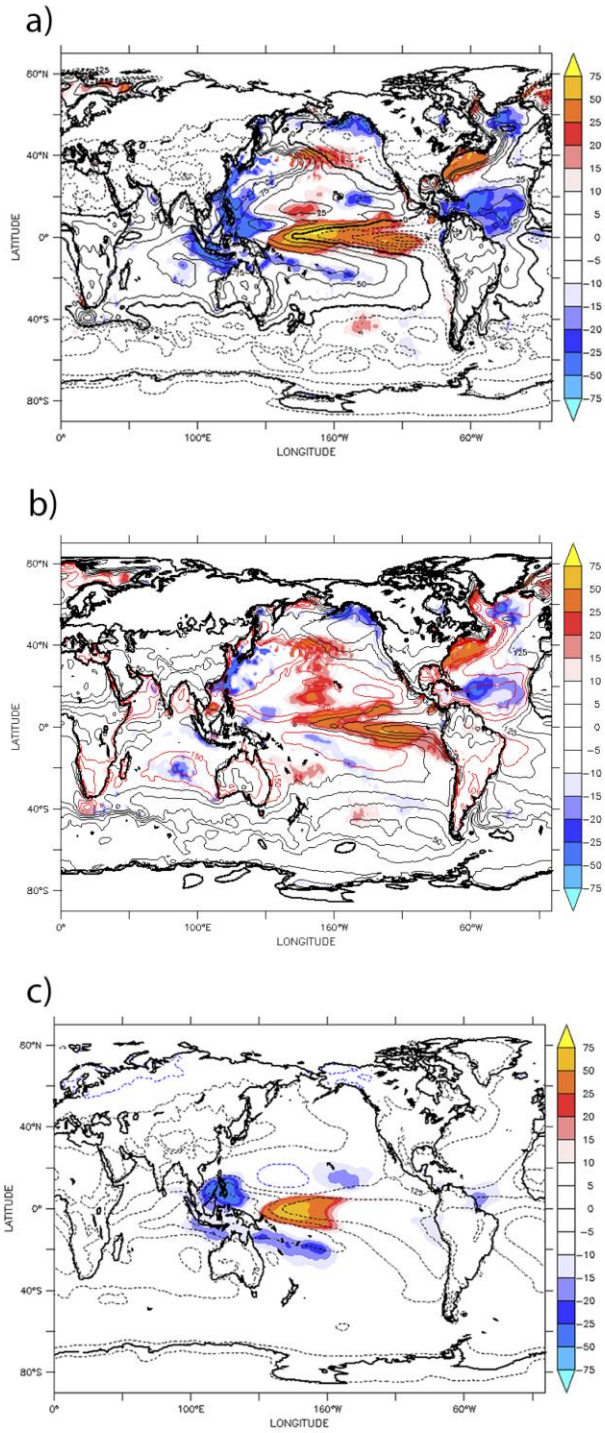


Fig. 10: El Niño minus La Niña condition composite differences of: a) the total MSE source, Q_{tot} (shading; in units of W m^{-2}); b) the surface turbulent flux component, Q_{surf} ; and c) the column radiative flux component, Q_{rad} . In each panel, line contours depict the MSE source for La Niña phase conditions, with a contour interval of 25 W m^{-2} and with solid (dashed) contours

1051 corresponding to positive (negative) values. Contours greater (less) than or equal to 150 W m^{-2}
1052 (-150 W m^{-2}) are highlighted in red (blue) for emphasis.
1053

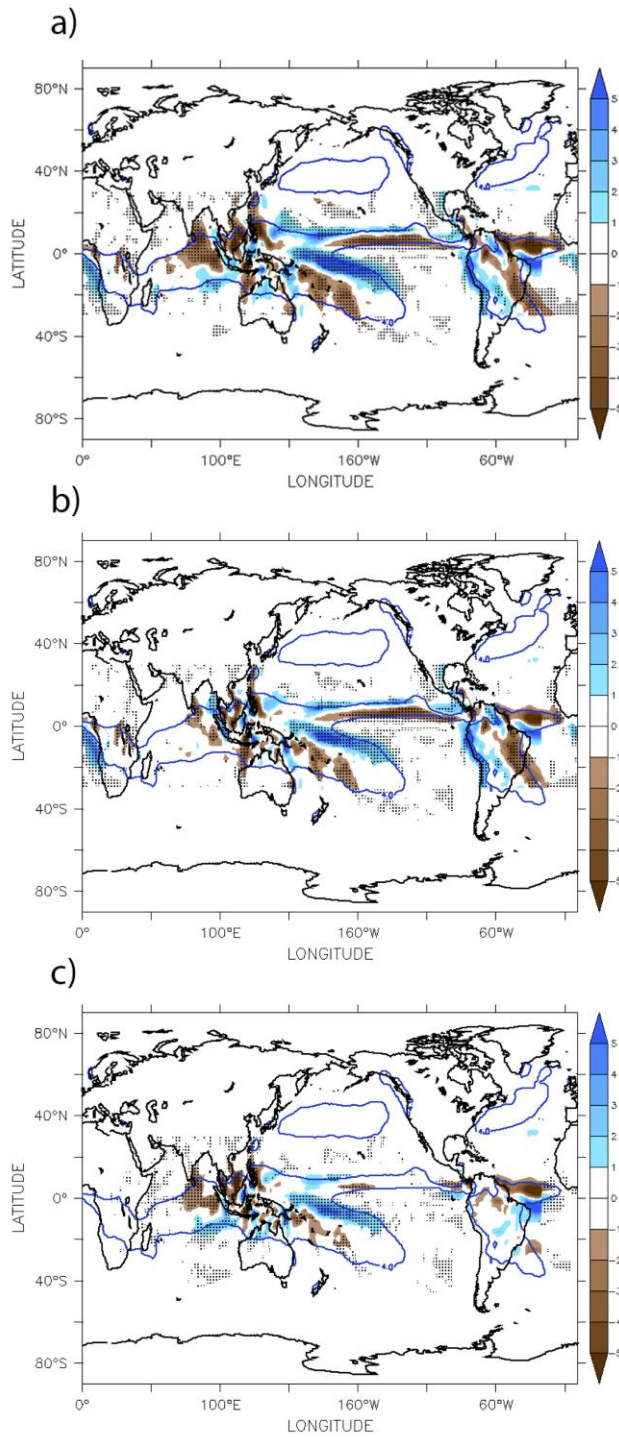


Fig. 11: El Niño (theory) minus La Nina condition composite precipitation differences, as in Figure 5a, but computed for: a) Qtot; b) Qsurf only; and c) Qrad only.

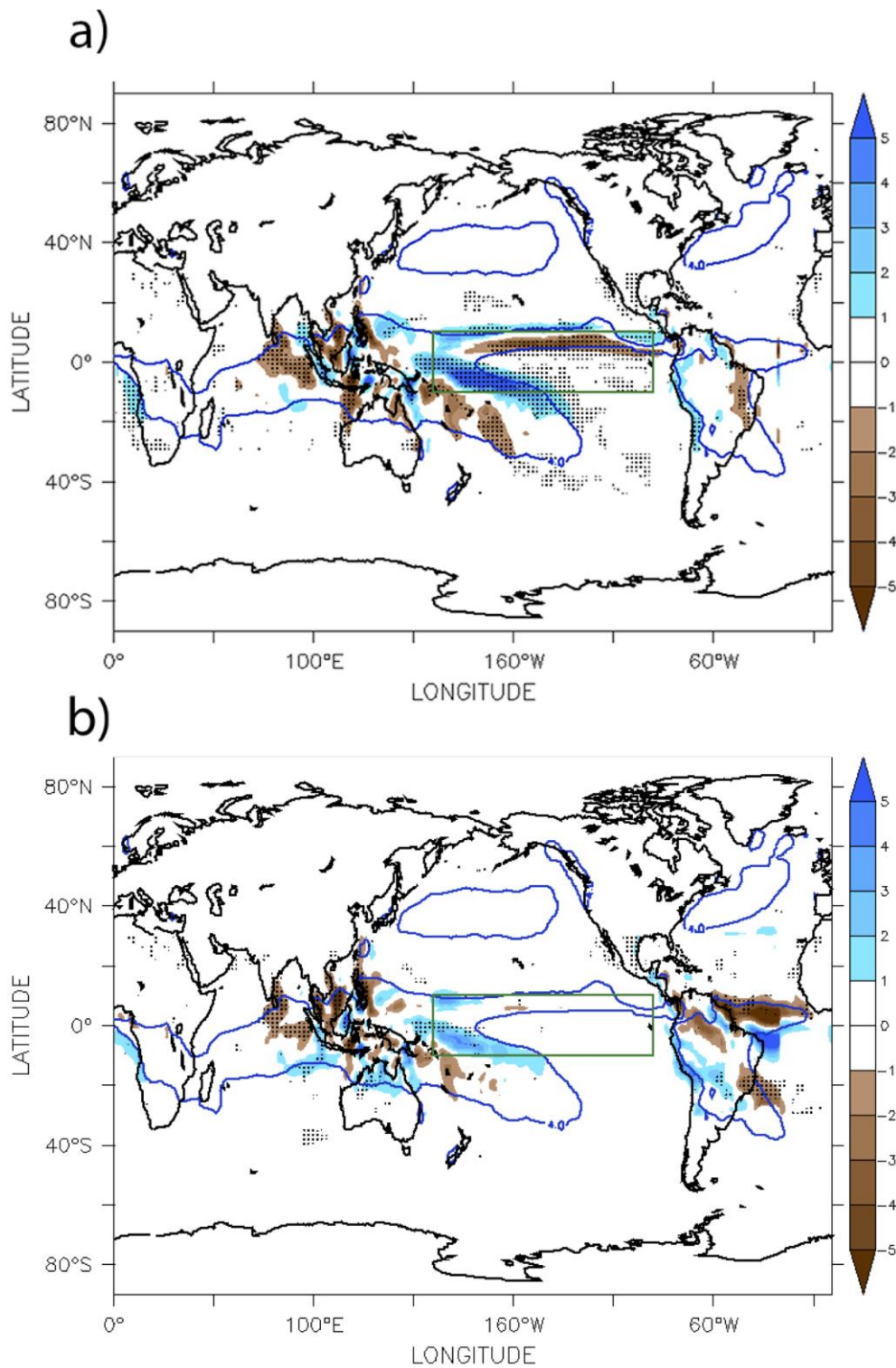


Fig. 12: El Niño (theory) minus La Nina condition composite precipitation differences, as in Figure 5a, but for: a) MSE sources confined to the ENSO source region area only (the area within the green box); and b) MSE sources outside of the green box.